

1 **Alongshore variability in wave energy transfer to coastal cliffs**

2

3 **E.C. Vann Jones\*, N.J. Rosser and M.J. Brain**

4

5 Department of Geography, Durham University, South Road, Durham, DH1 3LE, UK

6

7 \*Corresponding author, email: [e.c.vann-jones@durham.ac.uk](mailto:e.c.vann-jones@durham.ac.uk)

8 **Abstract**

9           The alongshore distribution of wave energy is believed to be an important control on the  
10 spatial variability of coastal erosion. There is, however, a lack of field data quantifying the  
11 alongshore variability in wave energy on rock coasts, whereby the relative control of coastline  
12 geometry versus foreshore characteristics on wave energy delivery remains unclear. A number of  
13 studies have identified high-frequency cliff-top ground shaking to be generated by wave impacts at  
14 the cliff toe during high tides (HT). To capture the variability of wave-cliff impact energy along-coast,  
15 we installed an array of cliff-top seismometers along a 1 km stretch of coastline in North Yorkshire,  
16 UK. Our aim is to constrain how wave energy transfer to the cliff toe varies, and to examine the  
17 relative energy transfer around typical coastline features, including a bay and headlands. Whilst the  
18 greatest HT ground motion energy is recorded at a headland and the lowest at the centre of the bay  
19 (5% of that observed at the headland), we identify no systematic alongshore variation in the HT  
20 ground motion energy that can be related to coastline morphology. We also note considerable  
21 variation between features of similar form: the total HT ground motion energy at one headland is  
22 only 49% of the next headland 1 km alongshore. Between neighbouring sites within the bay,  
23 separated by only 100 m, we observe up to an order of magnitude difference in ground motion  
24 energy transfer. Our results demonstrate the importance of the foreshore in driving the variations in  
25 energy delivery that we observe. Local alterations in water depth and foreshore topography control  
26 the alongshore distribution of wave energy available to generate cliff HT ground motions.  
27 Importantly, this apparently local effect overrides the influence of macroscale coastal planform  
28 morphology, which has previously been assumed to be the dominant control. The results show that  
29 foreshore characteristics that hold influence over wave energy transfer vary significantly over short  
30 (~100 m) distances, and so we expect erosion controlled by wave impacts to vary over similar scales.

31

32 **Keywords**

33           rock coast, coastal cliff, foreshore, microseismic, cliff shaking, wave impact

34

## 35 **1 Introduction**

36           The distribution of wave energy along coastlines is an important control on the spatial  
37 variability of erosion (e.g. Sallenger et al., 2002; Murray and Ashton, 2013). Understanding the  
38 interactions between coastal morphology and variable incident hydrodynamics is crucial to  
39 improving our understanding of the implications of future climate change and the potential changes  
40 in coastal erosion (e.g. Bray and Hooke, 1997; Walkden and Hall, 2005; Dickson et al., 2007;  
41 Trenhaile, 2011). The focussing of wave energy and erosion around rock coastlines is controlled by  
42 prevailing wave and current directions (Carter et al., 1990), the availability and distribution of  
43 sediment (Sunamura, 1976; 1982; Limber and Murray, 2011), coastline planform and foreshore  
44 geometry (e.g. Klein and Menezes, 2001; Bowman et al., 2009; Hapke et al., 2009; Limber and  
45 Murray, 2011; Limber et al., 2014), coastal bathymetry (e.g. Trenhaile, 1987; Komar, 1997), and  
46 relative rock strength and the resistance to wave energy transfer (Sunamura, 1977; 1992). Studies  
47 that examine the role of coastline geometry in determining wave energy and erosion focussing are  
48 largely based on field monitoring on softer rock coasts where both sediments and beach material  
49 play a dominant role in controlling erosion (e.g. Klein and Menezes, 2001; Sallenger et al., 2002;  
50 Bowman et al., 2009), which is also observed in numerical modelling studies of coastal change (e.g.  
51 Limber and Murray, 2011; Limber et al., 2014). Few studies, however, have examined the alongshore  
52 variability of wave energy transfer and erosion on low-sediment, rock coasts.

53           Recently a number of models have examined the long-term ( $\geq 1,000$  year) evolution of rock  
54 coast planform geometry and the driving processes that control morphology (e.g. Limber and  
55 Murray, 2011; Limber et al., 2014). In general, alongshore variations in shallow water bathymetry  
56 result in nearshore refraction of waves: the convergence of waves focuses energy onto headlands,  
57 and divergence disperses energy as waves enter bays (e.g. Trenhaile, 1987; Komar, 1997). Wave  
58 energy transfer to the coastline is therefore determined by the degree to which the coastline  
59 projects seaward and is thus more exposed to incoming waves and greater energies (Carter et al.,  
60 1990; Limber et al., 2014).

61           A number of field-based studies have calculated the energy available to erode rock  
62 foreshores and cliffs (e.g. Stephenson and Kirk, 2000; Trenhaile and Kanyaya, 2007), and have  
63 measured the distribution of wave energy cross-shore and the influence of foreshore characteristics  
64 (Ogawa et al., 2011; 2016; Poate et al., 2016; Stephenson et al., 2017). Such studies have not  
65 considered alongshore variability in these foreshore characteristics, the resulting wave energy  
66 dissipation and transfer to the cliff. The relative importance of planform geometry versus foreshore  
67 characteristics in determining how wave energy is distributed alongshore therefore remains  
68 unknown.

69 Coastal cliff-top ground motions have been observed by a number of recent studies to be  
70 generated by waves in the nearshore, the foreshore and at the cliff toe and distinct frequency bands  
71 of signals are observed (e.g. Adams et al., 2005; Young et al., 2011; 2012; 2013; 2016; Dickson and  
72 Pentney, 2012; Norman et al., 2013; Earlie et al., 2015; Vann Jones et al., 2015), which typically  
73 include: long-period ground motions ( $<0.05$  Hz/ $>20$  s) generated by infragravity waves on the  
74 foreshore/beach (e.g. Young et al., 2011; 2012); double frequency microseisms (0.1 – 0.2 Hz/5 – 10  
75 s) generated by the superposition of waves either in deep water, or following reflection from the  
76 coast which have a period half of that of the ocean waves (e.g. Longuet-Higgins, 1950); single  
77 frequency microseisms, generated by shallow-water waves as they interact with the seabed (e.g.  
78 Hedlin and Orcutt, 1989; Friedrich et al., 1998), where the frequency band is determined by shallow  
79 water wave periods, typically 0.1 – 0.05 Hz/10 – 20 s, although this has been shown to vary with  
80 local wave periods (e.g. Norman et al., 2013; Young et al., 2013); high frequency cliff shaking ( $> 1$   
81 Hz) is generated by wave impacts at the cliff toe (e.g. Vann Jones et al., 2015; Young et al., 2016) or  
82 foreshore edge (Dickson and Pentney, 2012) when tide heights allow. High frequency cliff shaking  
83 generated by wave-cliff impacts, have been found to provide a valuable proxy measurement of wave  
84 energy transfer directly to the cliff (Norman et al., 2013; Young et al., 2016), with statistically-  
85 significant relationships observed with monitored cliff erosion (Vann Jones et al., 2015). To date,  
86 cliff-top ground motion studies have largely focussed on single seismometers or on shore-normal  
87 transects of multiple seismometers (Dickson and Pentney, 2012; Young et al., 2012; 2013), yet given  
88 the sensitivity of data to nearshore wave conditions and cliff toe impacts, it is reasonable to assume  
89 that alongshore variations in wave impacts and loading will be reflected in commensurate variations  
90 in microseismic response.

91 The aim of this study is to constrain how wave energy transfer to the cliff toe varies  
92 alongshore, focussing in particular on the energy transfer around headland and bay morphology. We  
93 use these data to assess the relative control of coastline geometry versus foreshore characteristics  
94 on energy delivery. To achieve this, we deploy an array of cliff-top seismometers to capture the  
95 short-term alongshore variability in high-frequency cliff ground motion around a hard rock, low-  
96 sediment bay and headlands. Using high-frequency ground motions as a proxy for wave impacts, and  
97 thus energy transfer directly to the cliff toe, enables us to obtain a relative measure of wave energy  
98 delivery around the coast.

99

## 100 **2 Study site**

101 A 1 km stretch of coast between Staithes and Port Mulgrave on the NE Yorkshire coast, UK  
102 (Fig. 1) was selected as a site, to enable us to explore varying degrees of planform crenulation,

103 aspect and foreshore platform configuration. The monitored stretch of coast encompasses one bay  
104 ca. 570 m in width, and two adjacent headlands. The cliffs are 45 - 55 m high (Fig. 2a – g), comprised  
105 of near-horizontally interbedded Lower Jurassic shales, mudstones and limestones, capped with  
106 fine-grained sandstone and glacial till, which are uniform across the study site. The site has a wide  
107 (up to 300 m) rock foreshore (Fig. 2), and a high semi-diurnal tidal range (6 m). The cliff face  
108 exposure to waves and sea water varies considerably during the tidal cycle. During mean low spring  
109 tides the waterline can be up to 300 m from the cliff toe, but during mean high spring tides the still  
110 water level is ca. 1 m above the cliff toe. Dominant incoming wave directions are NE (Fig. 3j). Mean  
111 significant wave height ( $H_s$ ) for the study period was 0.95 m and maximum wave height ( $H_{max}$ ) was  
112 9.26 m (both measured 1.5 km from the coastline (data courtesy of North East Coastal Observatory)).  
113 The cliff morphology, foreshore topography and elevation vary along the coast, ranging from -2 m  
114 OD at mean low spring tide level, to the highest cliff toe elevation at 1.4 m OD at the centre of the  
115 bay (Figs. 1, 2).

116

### 117 **3 Methods**

#### 118 **3.1 Field data**

119 The following data were captured over an eight-month monitoring period (December 2013 –  
120 July 2014):

121 • Seven Güralp 3TP broadband seismometers were deployed in temporary wells dug into the  
122 glacial till at the cliff-top, positioned 10 m from the cliff edge, spaced at ca. 100 m intervals  
123 along the coast (ES01 – ES07, Fig. 1c). Ground motion velocities in three components (N – S, E –  
124 W, vertical (Z)) were sampled at 100 Hz. The flat frequency response of the seismometers is 120  
125 s – 50 Hz.

126 • At each site the foreshore profile normal to the cliff face was extracted from a high-  
127 resolution airborne LiDAR survey collected in 2015 at low tide (Fig. 1c). To extract a profile, the  
128 point cloud (ca. 60 ppm) was gridded using kriging to generate a DEM at 0.25 m resolution,  
129 from which a shore-normal profile was calculated at each instrument position (Figs. 1c, 2h-n).

130 • Monitored tide and wave heights (sampled every 15 minutes and 30 minutes, respectively)  
131 were obtained from a nearby tide gauge and wave buoy both at Whitby (ca. 13 km south east)  
132 (data courtesy of North East Coastal Observatory, [www.northeastcoastalobservatory.org.uk](http://www.northeastcoastalobservatory.org.uk)).  
133 The buoy is situated 1.5 km offshore and in a water depth of approximately 17 m. Monitored  
134 wind velocities were obtained from a nearby Met Office (2006) weather station at Loftus (ca. 5  
135 km west).

136

## 137 **3.2 Data processing and modelling**

### 138 **3.2.1 Seismic data**

139 The vertical component (Z) was used to avoid signal contamination due to ground tilt, which  
140 can adversely affect the horizontal motion recorded (e.g. Bormann, 2009; Young et al., 2012). Days  
141 containing noise due to instrument errors (e.g. loss of power), or maintenance periods, were  
142 removed. Data gaps varied between the instruments (Fig. 2a-g). Only time periods when all seven  
143 seismometers were working in parallel (95 days) were used in this analysis.

144 Ground motion velocity was bandpass-filtered to the frequency range 3.3 – 33.3 Hz, which  
145 we observed to represent cliff shaking caused by wave impacts at the cliff toe during high tides (HT)  
146 at this site. Previous studies have demonstrated that high-frequency cliff shaking, with the frequency  
147 range varying slightly between study locations, produces higher correlation coefficients with  
148 modelled and measured cliff toe wave conditions than microseism (MS) and long-period (LP)  
149 frequencies that represent wave loading in the nearshore and offshore (Norman et al., 2013, Vann  
150 Jones et al., 2015; Young et al., 2016). HT ground motion signals have also produced higher  
151 correlation coefficients with observed rockfall (Vann Jones et al., 2015).

152 Hourly statistics over the 95-day monitoring period describing HT ground motion energy  
153 ( $(\mu\text{m s}^{-1})^2$ ) are presented: hourly total ( $Total_h$ ), hourly maximum ( $Max_h$ ) and total energy over the  
154 monitoring period ( $Total$ ). The time series of HT ground motion energy was also aggregated by water  
155 elevation, derived from the modelled cliff toe water levels (see section 3.2.2.1 below), to assess  
156 energy transfer as a function of water depth and inundation duration (see section 4.3).

157

### 158 **3.2.2 Wave data**

#### 159 **3.2.2.1 Wave model**

160 In the absence of monitored cliff toe wave conditions, a linear wave model based on that of  
161 Battjes and Stive (1985) (see Norman et al., 2013) was used to transform wave heights measured at  
162 the wave buoy. Wave heights were transformed by shoaling and energy dissipation via turbulence as  
163 they break in decreasing water depths (calculated from the tide gauge time-series for the monitoring  
164 period) across the nearshore and foreshore profile normal to the cliff seaward of each seismometer  
165 (Fig. 2h-n). The model accounts for set-up and set-down as waves break but does not account for  
166 turbulence within surf bores after breaking, nor bed friction in the surf and swash zones. At each  
167 timestep, once waves had broken, wave heights for the remaining depth profile to the water's edge  
168 were set at the breaking wave height, which decreases with the water depth and therefore  
169 simulates further energy dissipation within the surf and swash zones. The model also does not  
170 account for energy dissipation due to wave refraction, reflection or diffraction. Although a 3D model

171 would be desirable because of the complex foreshore topography, this was not possible due to a  
172 lack of high resolution bathymetry data. Time series of combined tide and modelled wave elevation  
173 at the cliff toe ( $h_{elevation}$ , m OD) and combined tide and modelled wave height above the cliff toe  
174 ( $h_{height}$ , m) were then calculated for each profile to derive inundation elevation, water surface height  
175 above the cliff toe, and inundation frequency at each site.

176

### 177 **3.2.2.2 Model validation**

178 Whilst no monitoring of cliff toe/foreshore waves was available for the seismometer  
179 monitoring period, wave pressure sensors (WPS (RBR Solo D, sampling at 2 Hz for 2048 samples  
180 every 30 minutes)) were installed on the foreshore for 13 days (20 Feb – 4 Mar 2015) for a  
181 subsequent study. The WPS were positioned ca. 10 m from the cliff toe on the wave model profiles  
182 of ES02, ES04 and ES06 (within 10 m), and within 73 m from the profiles of ES05 and ES07. The WPS  
183 at ES02, ES04 and ES06 were used in the model validation.

184 There is a broadly linear relationship between the significant wave height ( $H_s$ ) observed and  
185 modelled for all three sites individually (Fig. 4a-c), and for all combined (Fig. 4d). This indicates that  
186 at ES01 and ES06 the wave model overestimates wave heights (Fig. 4a, c), whereas at ES04 it  
187 underestimates height (Fig. 4b). Differences between modelled and monitored wave heights  
188 increase with height, and the fewer wave heights over 1 m at ES04 and smaller sample size may  
189 explain why the relationship at ES04 is underestimated. The coefficient of determination of the  
190 relationship at ES04 is also lower ( $r^2 = 0.264$ ) than at ES01 ( $r^2 = 0.416$ ) and ES06 ( $r^2 = 0.343$ ), likely  
191 also because of the lack of larger  $H_s$  ( $> 1$  m). Differences in this relationship between sites illustrate  
192 the influence of the complex foreshore topography on the wave characteristics.

193

## 194 **4 Results**

### 195 **4.1 Observed cliff-top seismic signals**

196 Three distinct bands of marine-generated seismic signals are evident in the spectrograms for  
197 each instrument (Fig. 3): long period (LP) signals ( $>20$  s/ $<0.05$  Hz) assumed to be generated by  
198 infragravity waves on the foreshore; microseisms (MS) (1-20 s/ $1-0.05$  Hz) consisting of double  
199 frequency (DF) and single frequency (SF) microseisms; and high frequency shaking (0.03 – 0.3 s/ $3.33$   
200 – 33.33 Hz) attributed to wave impacts at the cliff toe during high tides (HT). Signal power for each  
201 band (LP, MS and HT) varies across the seven seismometers (Fig. 3). Commonly at this site we  
202 observe increases in HT signal power with corresponding increases in MS and LP signal power,  
203 indicative of stormier conditions with larger waves dissipating as they break across the foreshore  
204 and at the cliff during high tides and storm surges (Fig. 3). The highest HT signal power is observed at

205 ES06 (Fig. 3f), with a peak of  $\sim$ -65 dB. ES07 (Fig. 3g) and ES01 (Fig. 3a) have similar peak signal  
206 powers, but these peaks occur less frequently than at ES06. ES04 (Fig. 3d) has significantly fewer HT  
207 peaks than observed at the other sites, and the peak signal power is lowest (-70 dB).

208 To determine the sources of these ground motion signals and their proximity to the  
209 seismometers, we examine the signals over a range of incident tide and wave conditions (Figs. 5, 6).  
210 During a spring tide storm (Fig. 5a-i) ( $H_s = 3.15$  m, maximum wave height = 9.26 m, observed at the  
211 wave buoy) it is evident that both the LP and HT signal power is tidally modulated, whereby signal  
212 power increases and decreases with tide height (Fig. 5a-i). These signals are thus generated by the  
213 presence of sea on the foreshore and at the cliff. Increases in signal power in the LP signal precede  
214 those in HT (Fig. 5a-g), indicating the LP signal is generated across a wider area.

215 The lowest LP ground motion signal powers occur at ES07 (peak power of  $\sim$ -115 dB) (Fig. 5g),  
216 and the highest ( $\sim$  -105 dB) at ES05 and ES06 (Fig. 5e, f). At ES05, ES06 and ES07, increased signal  
217 powers in the LP band also occur during low tides (Fig. 5e-g), assumed to be generated by  
218 infragravity waves on the foreshore. The duration and power of these signals represents the  
219 effectiveness of the foreshore near these locations in either releasing infragravity energy via wave  
220 breaking, or the propagation of infragravity energy tied to swell wave groups across the foreshore.

221 The tidal modulation of HT can be seen clearly at all sites in the power spectrograms  
222 captured during the storm and spring tide example (Fig. 5a-i). Ground motion signal power varies  
223 across the seven instruments, with highest values ( $\sim$ -60 dB) observed at the headlands, ES01 (Fig. 5a)  
224 and ES06 (Fig. 5f). During the low tides, the HT signal power is higher than during non-storm  
225 conditions (Fig. 5j-r) where it is absent, suggesting that the storm surges raise water levels up the  
226 foreshore and towards the cliff, generating wave impacts on the foreshore more proximal to the cliff  
227 toe. ES01 (Fig. 5a), ES06 (Fig. 5f) and ES07 (Fig. 5g) have higher HT signal powers during the low tides  
228 in the storm than at the other sites, which suggests that in these locations waves are able to break  
229 closer to the cliff.

230 The shorter duration of the peaks in HT ground motion signal powers compared to the LP  
231 signal powers corresponds to the deepest water levels at the cliff toe at each site ( $> 2$  m OD) (Fig. 5a-  
232 g), indicating HT ground motion is generated by waves impacting against the cliff face during  
233 elevated water levels. At ES06  $h_{elevation}$  (Fig. 5h) exceeds the cliff toe around 1 – 2 hrs earlier than at  
234 the other sites because it has the lowest cliff toe elevation (-0.62 m OD). ES06 thus is subject to the  
235 deepest cliff toe water depths (6.44 m OD) enabling larger waves to reach the cliff (Fig. 5h).

236 ES04 (Fig. 5d) has the lowest HT ground motion signal power, and a more pronounced binary  
237 distinction in the signal between high and low tides, indicating that waves only become  
238 microseismically detectable, and therefore perhaps erosively effective, during the highest tidal



239 elevations. ES04 has the shortest duration of inundation (Fig. 5h), the highest cliff toe elevation (1.4  
240 m OD), and as a result, the lowest peak  $h_{elevation}$  (4.76 m OD) (Fig. 5h).

241 Higher MS signal powers occur at ES05, ES06 and ES07 during storm conditions (Fig. 5e-g)  
242 (peak power of ~80 dB compared to peaks of -92 dB at ES01 – ES04, Fig. 5a-d). During the high tides,  
243 the MS signal powers at ES05 – ES07 also extend across a wider range of periods, from 20 s to <1 s,  
244 where the MS ground motion signals merge with the HT ground motion signals (Fig. 5e-g).  
245 Differences in MS signal powers between the sites demonstrate that some of the MS signal power  
246 must be generated by gravity waves on the foreshore/in the nearshore local to each seismometer.

247 During less energetic spring tides ( $H_s = 1.05$  m, maximum wave height = 3.5 m at the wave  
248 buoy) (Fig. 5j-r) the HT and LP ground motion signals are still evident during each high tide at all 7  
249 sites, however the HT and LP signal power values and durations are lower and shorter compared to  
250 the storm spring tide example (Fig. 5a-g). At ES06 (Fig. 5o) the peak HT signal power is 15 dB lower  
251 and the peak LP signal power is 25 dB lower, and approximately three hours shorter. Both the LP and  
252 HT signal powers are weakest during the second high tide (Fig. 5j-p) when peak tide elevation is 3.1  
253 m OD (Fig. 5q) and peak  $H_s$  is 0.8 m (Fig. 5r). The wave heights are similar to those during the first  
254 tide of the storm example (Fig. 5i) when the HT and LP seismic signals are absent (Fig. 5a-g), however  
255 the higher tide elevation (Fig. 5q) enables the HT signal to be generated. It is therefore the  
256 combination of tide and wave height that are important to the generation of HT. Differences in HT  
257 signal power between sites are more apparent during less energetic conditions (Fig. 5j-p) than  
258 during the storm example (Fig. 5a-g).

259 During stormy neap tides ( $H_s = 1.88$  m, maximum wave height = 6.09 m at the wave buoy)  
260 the HT and LP ground motion signals are only evident during high tides (peak = 1.85 m OD) when  $H_s$   
261 is ~ 2 m (Fig. 6a-i). The signal power and duration of the LP signals is lower and shorter (for example  
262 at ES06 ~10 dB lower and ~three hours shorter, Fig. 6f) than during the spring tide storm (Fig. 5a-g),  
263 as lower tide heights and a smaller storm surge result in shorter foreshore, and cliff inundation  
264 durations. Smaller wave heights result in lower signal power across the marine-generated seismic  
265 signals. The HT signals are less clearly defined and lower power than both spring tide examples (Fig.  
266 5) (e.g. ~20 dB lower at ES06).

267 During low wave energy neap tides ( $H_s = 0.32$  m, maximum wave height = 0.76 m) (Fig. 6j-r)  
268 there are no HT or LP ground motion signals. In the absence of the HT seismic signals, it is evident  
269 there is also high frequency shaking generated by wind (WI), particularly when velocities exceed ~ 7  
270  $\text{ms}^{-1}$  at frequencies  $\geq 10$  Hz/ $\leq 0.1$  s (Fig. 6r). The WI signal overlaps with the higher frequencies of  
271 the HT signal, however the WI signal is only generated during above-average wind velocities, and the  
272 spring tide examples (Fig. 5) demonstrate that the HT signal dominates the 3.3 – 33.3 Hz band. The

273 difference in ground motion signals between the sites demonstrates that these signals are generated  
274 locally to each seismometer and that the sea conditions generating them vary across distances of <  
275 79 m (the shortest distances between neighbouring seismometers).

276

#### 277 **4.2 Observed alongshore distribution of HT ground motion energy**

278 The remainder of the analysis focuses on the HT ground motion signals to examine  
279 alongshore differences in wave-cliff impacts. The eastern headland in our study site, ES06,  
280 experiences the greatest HT ground motion energy in all metrics presented (Fig. 7): *Total* ( $4.22 \times 10^{14}$   
281  $(\mu\text{m s}^{-1})^2$ ) (Fig. 7a); *Max<sub>h</sub>* ( $117 \times 10^3 (\mu\text{m s}^{-1})^2$ ) (Fig. 7b) and 99<sup>th</sup> percentile of the *Max<sub>h</sub>* ( $10.7 \times 10^3 (\mu\text{m}$   
282  $\text{s}^{-1})^2$ ) (Fig. 7c).

283 ES07 has the second highest value of *Total* ( $2.67 \times 10^{14} (\mu\text{m s}^{-1})^2$ ), just over half that at ES06  
284 (Fig. 7a). The *Max<sub>h</sub>* at ES07 is the lowest ( $3.1 \times 10^3 (\mu\text{m s}^{-1})^2$ ) (Fig. 7b), indicating it is average wave  
285 conditions here that are more energetic relative to sites ES01 - ES05, rather than the extreme  
286 events.

287 Whilst ES05 has a high relative *Max<sub>h</sub>* value ( $104.8 \times 10^3 (\mu\text{m s}^{-1})^2$ ) (Fig. 7b), the 99<sup>th</sup> percentile  
288 ( $3.2 \times 10^3 (\mu\text{m s}^{-1})^2$ ) (Fig. 7c) indicates an outlier, the *Total* (Fig. 7a) is the third lowest, indicating it is  
289 actually a relatively low HT ground motion energy site. Site ES04 which lies at the centre of the bay  
290 has the lowest of all the measures of HT ground motion energy, with *Total* =  $0.21 \times 10^{14} (\mu\text{m s}^{-1})^2$  (Fig.  
291 7a) 5% of that received at ES06. ES02 is also a relatively low-energy site, with the second lowest  
292 measures of HT ground motion energy (excluding *Max<sub>h</sub>*) and *Total* =  $0.46 \times 10^{14} (\mu\text{m s}^{-1})^2$ , 12% of that  
293 at ES06 (Fig. 7a).

294 ES01, the western headland, has the largest *Max<sub>h</sub>* HT ground motion energy ( $118 \times 10^3 (\mu\text{m}$   
295  $\text{s}^{-1})^2$ ) (Fig. 7b), but the 99<sup>th</sup> percentile suggests this is, again, an outlier ( $5.8 \times 10^3 (\mu\text{m s}^{-1})^2$ ) (Fig. 7c).  
296 The *Total* HT ground motion energy ( $1.95 \times 10^{14} (\mu\text{m s}^{-1})^2$ ) is similar to that at ES03 ( $2.15 \times 10^{14} (\mu\text{m s}^{-1})^2$ ) (Fig. 7a), which lies at the centre of the bay.

298

#### 299 **4.3 Controls of the observed alongshore variability in HT ground motion energy**

300 The observed variability in microseismic ground motions implies that conditions that  
301 determine wave characteristics and energy delivery to the cliff toe vary between the seven positions  
302 monitored. The marine controls on signal variability are tested by examining the effects of both  
303 marine and foreshore variables. We consider cliff toe elevation, foreshore characteristics, tide and  
304 wave heights, and examine the effects of these on the ground motion signals recorded by the seven  
305 instruments.

306 Cliff toe elevation varies over 2.02 m between sites and is a key control of energy transfer to  
307 the cliffs (Fig. 8). ES06 experiences inundation over the greatest elevation range ( $R_{ind}$ , 8.2 m) and has  
308 the lowest cliff toe elevation (-0.62 m OD), a steep, narrow and smooth foreshore, conducive in form  
309 to ramping waves up-cliff (Fig. 8k). The greatest HT ground motion energy over the monitoring  
310 period (Figs. 7, 8l) is observed here. ES04 has the highest cliff toe elevation (1.4 m OD) and the most  
311 constricted range in inundation ( $R_{ind} = 4.7$  m) (Fig. 8g), with lower tide water depths and thus wave  
312 heights. This instrument records the lowest HT energy (Figs. 7, 8h), indicating that significant wave  
313 energy dissipation occurs before waves reach the cliff toe at this location. Where foreshore  
314 topography enables waves to break closer to or at the cliff, more wave energy is transferred into cliff  
315 as HT ground motion.

316 The vertical distribution of *Total*, derived from  $h_{elevation}$ , varies between sites but again shows  
317 no systematic alongshore pattern that mirrors the coastal planform (Fig. 8). The foreshore profiles  
318 show that not only cliff toe elevation but also foreshore topography and width vary considerably  
319 between the seven sites (Figs. 2, 8). Peaks in *Total* (Fig. 8b, d, f, h, j, l, n) typically coincide with water  
320 levels at elevations most frequently inundated by  $h_{elevation}$ , or the zone just above (ES01 - 3, ES06 - 7),  
321 and broadly reflect the vertical inundation duration below 5 m OD (Fig. 8a, c, e, g, i, k, m). At all sites  
322 there is also an increase in *Total* when  $h_{elevation}$  inundation is at its maximum in the largest albeit  
323 rarest storms. At sites ES02, ES04 and ES05, this is when the highest *Total* occurs (Fig. 8). ES02, ES04  
324 and ES05 are the lowest HT ground motion energy sites suggesting that when the water level is at  
325 the more frequently inundated elevations of the cliff face, most incident wave energy is dissipated  
326 across the foreshore before reaching the cliff toe and that only during the largest storm events can  
327 significant energy be transferred to the cliff at these sites.

328 At the sites which experience more energetic HT ground motions (ES06, ES07, ES03 and  
329 ES01) the vertical distribution of *Total* suggests that significant wave energy is transferred to the cliff  
330 throughout the tidal inundation cycle. Therefore, less wave energy is dissipated across the foreshore  
331 in front of the cliff in these locations. At these sites, the peak *Total* occurs at different elevations,  
332 likely representing the varying foreshore characteristics, and the resulting differences in shoaling of  
333 the incident wave field. As foreshore geometry varies in a non-systematic manner between adjacent  
334 sites, it is clearly a key control on the transfer of wave energy, influencing cliff microseismic  
335 excitation.

336 To examine the effect of cliff characteristics on the HT ground motion signal recorded at  
337 each seismometer, such as signal attenuation or amplification, and to determine the relative  
338 influence of these on *Total* compared to foreshore characteristics, metrics describing cliff and

339 foreshore topography were correlated with *Total* (Fig. 9). Those that derived statistically-significant  
340 relationships ( $p$ -value  $\geq 0.05$ ) with *Total* are presented in Fig. 9.

341 Cliff toe elevation (Fig. 9a), the number of foreshore steps (Fig. 9b), and foreshore elevation  
342 range (Fig. 9c), all have a negative linear relationship with *Total* ( $r^2 \geq 0.67$ ). The linear distance  
343 between the seismometer and the cliff toe, and along the cliff face, demonstrate positive linear  
344 relationships with *Total* ( $r^2 = 0.80$  and  $0.78$  respectively, Figs. 9d, e), whilst the mean and maximum  
345 cliff slope have negative linear relationships ( $r^2 = 0.93$  and  $0.84$ , respectively, Figs. 9f, g). The  
346 relationship between the seismic signal amplitude and both cliff slope and distance are the inverse  
347 of what would be expected if local cliff topography dominate the HT seismic signal amplitude (e.g.  
348 Ashford et al., 1997; Messaudi et al., 2012). These results demonstrate that the relative amplitude of  
349 the HT ground motion signal alongshore is, on the whole, not determined by the effects of local cliff  
350 topography. Instead, the HT signal recorded is dominated by the microseismicity resulting from the  
351 interaction of the sea and the cliff toe, which in turn reflects the local variability in the foreshore  
352 characteristics (Fig. 9). This demonstrates that using the current seismometer array/set-up at this  
353 site, the HT ground motion signal provides a valuable representation of marine conditions at the cliff  
354 toe local to the seismometer and enables alongshore comparison of HT signal amplitudes.

355 At all seven sites there is an apparent threshold of the combined tide and wave height above  
356 the cliff toe ( $h_{height}$ , m) at 2 m, above which there is an absence of smaller HT ground motion energy  
357 events and  $Total_h$  energy increases with  $h_{height}$  (Fig. 10). Despite the scatter in the data, on average  
358 we observe an order of magnitude increase in  $Total_h$  between  $h_{height}$  of 5 m and 7 m, increasing from  
359  $10 \times 10^{11} (\mu\text{m s}^{-1})^2$  to  $10 \times 10^{12} (\mu\text{m s}^{-1})^2$ . A similar behaviour above 2 m at all sites may suggest that  
360 water depths during the large storm events are deep enough that the local foreshore effects on  
361 wave shoaling are effectively over-written, whereby a more uniform microseismic response is  
362 observed at all instruments.

363

## 364 **5 Discussion**

### 365 **5.1 Overview of findings**

366 We find HT ground motions reflect variations in foreshore topography and mirror the  
367 resulting variability in wave energy dissipation. We show distinct differences between the  
368 microseismic excitation of cliffs within bays and headlands. The observed microseismic ground  
369 motion is shown to encompass the complexity of nearshore wave climate, including refraction,  
370 foreshore and cliff toe characteristics, into a single measure, providing a relative measure of energy  
371 delivery to the cliffs.

372

373 **5.2 The influence of foreshore morphology on HT ground motion energy**

374 The alongshore distribution of HT microseismic energy is highly variable, with no pattern  
375 that obviously maps onto the bay - headland planform coastline geometry. Our results demonstrate  
376 the importance of the foreshore modification of waves in driving energy transfer to the cliff, which  
377 potentially then maps onto the resultant erosion response. Local alterations in water depth and  
378 foreshore topography play a key role in the alongshore distribution of wave energy that is available  
379 to generate cliff HT ground motions, and over-rides that of macroscale planform coastline geometry.  
380 Importantly the results show that these foreshore characteristics vary significantly over only short  
381 distances, here ca. 100 m. The exact position of a seismic monitoring station along a coast therefore  
382 holds a considerable influence on the nature of the HT ground motion signals that will be observed.

383 Cliff toe and foreshore elevation relative to the tidal range determines water depths and  
384 thus wave heights at the cliff and locations of wave breaking. The different elevations of the cliff toe  
385 across the monitored 1 km coastline examined here, relative to the macrotidal range (6 m), result in  
386 significant variability in high tide water depths (modelled maximum of 2.88 – 4.9 m above the cliff  
387 toe) and thus wave heights (modelled maximum wave heights of 2.03 - 3.44 m). These observations  
388 match those of recent studies that have used transects of pressure sensors to measure the cross-  
389 shore distribution of wave energy, and the corresponding wave spectra, on rock foreshores. Both are  
390 dependent on the foreshore morphology and cliff toe elevation relative to the tidal range (Ogawa et  
391 al., 2011 & 2016; Poate et al., 2016; Stephenson et al., 2017). At sites with large macrotidal ranges  
392 (i.e. >7 m) during high tides and average wave conditions, pressure sensor data have shown the  
393 wave breakpoint to move landwards across the foreshore as tide levels rise (Poate et al., 2016;  
394 Stephenson et al., 2017) and increased corresponding wave energy density cross-shore (Stephenson  
395 et al., 2017). This effect can be seen at ES06 where the low cliff toe elevation and resulting deeper  
396 waters enable waves to break closer to/at the cliff as compared to at the other instrument locations  
397 (Fig. 2). In contrast the wide extent of high elevation foreshore at ES01, and resulting shallow water  
398 depths, means that waves break further away from the cliff than at the other sites (Fig. 2).

399 In a study of six microtidal platforms, Ogawa et al. (2016) found platform width and  
400 elevation to be dominant controls on wave energy reaching the cliff toe. More narrow and lower  
401 elevation platforms enable greater gravity wave energy to propagate across the platform due to  
402 greater water depths (Ogawa et al., 2016), which matches our observations where the greatest HT  
403 ground motion energy occurs at ES06. At higher elevation and wider microtidal platforms, greater  
404 gravity wave energy is dissipated across the platform and the ratio of infragravity to gravity energy  
405 increases towards the cliff due to the shallow water depths (Beetham and Kench, 2011; Ogawa et al.,  
406 2016). However, at East Staithes, foreshore width did not derive a statistically significant relationship

407 with HT ground motion energy observed at the cliff. This may be due to the complex foreshore  
408 topography, the presence of multiple steps, and the variability in between the seven instrument  
409 locations. Using pressure sensors across a ~300 m-wide macrotidal platform (11 m range),  
410 Stephenson et al. (2017) observed that high tide water depths enabled waves <2 m to travel  
411 unbroken across the platform, which only begin to break near the cliff toe, producing a narrow surf  
412 zone at the inner foreshore. At microtidal sites Marshall and Stephenson (2011) also found  
413 foreshore width to have a lesser influence on wave energy dissipation across the foreshore than  
414 foreshore gradient and water depths.

415 The relative importance of foreshore gradient is determined by elevation relative to the tidal  
416 range, in addition to the tidal range itself. The importance of gradient and width may thus change  
417 throughout the tidal cycle (Ogawa et al., 2016), and hence here between sites. The role of foreshore  
418 gradient is also complicated by the variability cross-shore by, for example, the presence of steps.  
419 This is confounded by the common simplification to use one value for a whole site, which may not  
420 be representative of the whole platform width, as would be the case at East Staithes. In this study,  
421 sites of low foreshore roughness (here measured as the number of steps, given the minimal boulder  
422 coverage on the foreshore on this section of coast) experience lower cross-shore wave energy  
423 dissipation relative to the other sites, also observed at other macrotidal rock foreshores by Poate et  
424 al. (2016).

425 Differences in MS and LP signal power between sites demonstrates the effect of the varied  
426 foreshore morphology on wave energy dissipation. Higher MS and LP signal power at sites indicates  
427 the foreshore is conducive for propagating higher amounts of infragravity and gravity wave energy  
428 across the foreshore. The differences in HT total energy between sites, which exhibit similar MS/LP  
429 ground motion signals, indicate that foreshore characteristics near the cliff toe play a key role in  
430 dissipating wave energy and determining whether waves have already broken at the instant when  
431 they impact against the cliff toe.

432 Our results show that HT ground motion energy across the seven sites becomes more similar  
433 in character during an extreme storm, as compared to low energy, or indeed average, conditions  
434 (Figs. 5, 6). The difference in water depths and modelled wave heights at the toe of the seven sites,  
435 however, suggests that the levels of HT ground motion energy recorded at the seven sites during the  
436 storm do not represent similarities in wave heights, but instead may indicate similarities in wave-cliff  
437 face interaction, such as a more uniform pattern of waves breaking onto the cliff toe. At Scots Bay in  
438 the Bay of Fundy, another macrotidal site, during storm conditions Trenhaile and Kanyaya (2007)  
439 observed narrowing surf zones, lower levels of wave attenuation and more energetic types of  
440 breaking waves (plunging breakers) in the upper foreshore during high tides. This was compared to

441 the lower platform during lower tide levels and was attributed to greater water depths and higher  
442 platform gradients at the upper foreshore. Our results may suggest that similar cross-shore shifts in  
443 wave characteristics occur at our site during large storms, and that water depths are sufficiently  
444 deep that the effects of the variable foreshore characteristics between sites are negated, and  
445 therefore so too are the differences in wave breaking across the foreshore. We identify a threshold  
446 of ca. 2 m above the cliff toe (Fig. 10), above which we suggest conditions assimilate across the  
447 seven sites, as less wave energy dissipation occurs and more waves break directly against the cliff  
448 toe to generate HT cliff shaking.

449

### 450 **5.3 The influence of coastline geometry on HT ground motion energy**

451 Using HT ground motion energy as a proxy for wave energy transfer to the cliff toe, we  
452 demonstrate that at this hard rock, low-sediment coast, the relative energy observed at different  
453 positions alongshore is determined more by foreshore characteristics than the macro-scale coastline  
454 planform morphology. Coastline planform may rather be more influential in determining the  
455 difference in HT ground motion energy at the two headlands. Carter et al. (1990) and Limber et al.  
456 (2014) observed from field studies and modelling that energy observed at headlands is determined  
457 by the degree of coastline projection seaward, and thus exposure to incoming waves. At this study  
458 site, the ES06 headland protrudes slightly further from the bay as compared to the ES01 headland,  
459 and to the east of ES06 and ES07 the coastline drops away to the south (Fig. 1). Whilst both  
460 headlands are exposed to the dominant north-easterly waves, the greater projection seaward, and  
461 the southerly orientation of the coast to the east of the headland ES06 (Fig. 1), means that this site is  
462 exposed to a greater range of wave directions than ES01.

463 In Limber et al.'s (2014) numerical wave transformation model, headlands that protrude  
464 further induce greater wave refraction and convergence, and thus receive greater wave energy via  
465 wave-rock impacts. Whilst the greatest energy occurs at headland ES06 in our study, the lower  
466 foreshore elevation and deeper waters around the headland mean that during the dominant NE  
467 wave directions there is actually little wave refraction around the headland itself (Fig. 1d), and rather  
468 greater energy is due to the higher water depths around the headland. The difference in foreshore  
469 characteristics at ES06 and ES01 may in part be due to their relative exposure to the incident wave  
470 field and the resulting erosion of the foreshore. The coastline characteristics also likely explain why  
471 ES07, on the eastern flank of the ES06 headland, has the second highest energy total, and supports  
472 Komar's (1985) suggestion that greatest energy would be expected at the headland point (ES06). The  
473 geometry of the two headlands is also different, with ES01 being wider alongshore, shorter cross-  
474 shore and more rounded in planform. ES06 is narrower, longer and similar to the 'needle-like'

475 headlands characterised by Komar (1985). Interestingly, the relative energy and platform  
476 morphologies is counter to that observed by Carter et al. (1990) in Nova Scotia, who found stubby,  
477 rounded headlands to form in more exposed, higher energy positions.

478

#### 479 **5.4 Cliff ground motions as proxies of cliff toe wave energy**

480 This study builds on the previous body of work using single cliff-top seismometers that have  
481 demonstrated high frequency cliff shaking to be a valuable proxy of relative wave energy transfer to  
482 the cliff toe (Vann Jones et al., 2015; Young et al., 2016). We have demonstrated that the magnitude  
483 of cliff toe wave impact generated ground motions varies significantly alongshore and even over  
484 short distances (here ~100 m).

485 The wave-cliff impact signal (HT) frequency range varies between this and other  
486 microseismic studies globally (e.g. >0.3 Hz (Young et al., 2011), 7 – 20 Hz (Dickson and Pentney,  
487 2012), 1.1 – 50 Hz (Norman et al., 2013; Vann Jones et al., 2015), 20 - 45 Hz (Young et al., 2016)).  
488 Young et al. (2013) observed a range of bands between 2 – 40 Hz across a variety of soft and hard  
489 rock cliffs globally. The range of frequency bands observed indicates differences in site response to,  
490 and local effects on, wave-cliff impacts. Young et al. (2013) attribute the variability in site response  
491 to combinations of tide elevation, wave energy, site morphology and geology and local signal decay.  
492 Rock foreshores clearly complicate wave-cliff impact microseismic signals and result in significant  
493 variations between even contiguous sites because of the feedbacks between the foreshore and  
494 wave breaking and attenuation. Key to this is the elevation relative to the tidal range, and thus  
495 where waves break relative to the cliff toe. For example, at a meso-tidal site of high foreshore  
496 elevation relative to the high tide level, Dickson and Pentney (2012) observed the wave-cliff impact  
497 signal to be generated during low tides as waves broke at the steep seaward edge of the foreshore  
498 and shallow depths across the platform dissipated wave energy before reaching the cliff toe.

499 The exact area of signal generation at the cliff toe is unknown and further work is required  
500 to examine concurrently monitored cliff toe and foreshore wave conditions and cliff-top ground  
501 motions, to improve our understanding of cliff toe waves. However, the differences in HT signals  
502 between sites in this study demonstrate that the HT signals are generated by cliff-wave impacts local  
503 to each seismometer, whereby small distances along coast can result in very different behaviours  
504 observed.

505 Some of the variation observed in ground motion energy across the sites must be  
506 considered a function of local site and instrument effects, which influence to some degree signal  
507 attenuation and amplification, including instrument-ground coupling, cliff material and structure  
508 (Lowrie, 1997; Stein and Wysession, 2003), topography (Ashford et al., 1997), and moisture content



509 (Mavko et al., 1998). However, identifying, testing and quantifying these effects on the signals and  
510 calibrating signals recorded at each site remains challenging. In simple analysis of the relationship  
511 between HT signal energy and cliff morphology, such as the slope and distance from seismometer –  
512 cliff toe, we found the HT signal to be dominated by cliff toe wave conditions, which are of a  
513 magnitude that dominates any influence of instrument position or highly local site effects in our  
514 array (e.g. Ashford et al., 1997; Messaudi et al., 2012). Inevitably, with more structural, geological or  
515 topographic variability between sites, such effects must at some point become significant.

516 HT ground motion signals have been found to have the strongest correlations with observed  
517 cliff face erosion, as compared to microseism (MS) and long period (LP) frequency bands (Vann Jones  
518 et al., 2015). As a result, we argue that our findings may have important implications for how wave-  
519 driven cliff erosion is distributed alongshore and more work is required to examine this further.

520

## 521 **6 Conclusions**

522 High frequency cliff motions (HT) generated by wave-cliff impacts provide a valuable proxy  
523 measure of the relative wave energy transfer along a coast at the cliff toe. Using an array of seven  
524 cliff-top seismometers placed at ca. 100 m intervals along a 1 km stretch of coastline, we quantified  
525 the alongshore distribution of relative wave energy transfer. There is no systematic alongshore  
526 pattern in microseismic HT ground motion energy recorded by the seismometers during the  
527 monitoring period around the bay and headlands study site. The greatest HT ground motion energy  
528 occurs at a headland and the lowest at the centre of the bay (5% of the headland). However, there is  
529 an order of magnitude difference in total HT ground motion energy between some neighbouring  
530 sites within the bay, and the two headlands experience very different relative HT ground motion  
531 energies (energy at the eastern headland is 49% of the western headland). We suggest that the  
532 significant variations in foreshore characteristics observed here are responsible for the alongshore  
533 variations in the (modelled) cliff toe water elevations and corresponding HT ground shaking energy  
534 observed. Importantly, the effect of the foreshore on wave energy dissipation overrides the  
535 influence of macroscale coastal planform geometry. We suggest that the alongshore variability in  
536 wave energy focussing over short distances controlled by local variability in foreshore characteristics  
537 that we observe will inevitably hold important implications for the distribution of resulting cliff  
538 erosion, and more work is required to examine this further.

539

## 540 **Acknowledgements**

541 The authors gratefully acknowledge the funding for this research provided by ICL (Fertilizers)  
542 Ltd. UK. The seismic equipment was provided by NERC's SEIS-UK (loan number 985) and the authors

543 are grateful for support provided by Victoria Lane and David Hawthorn. Wave and tide data are  
544 courtesy of the North East Coastal Observatory ([www.northeastcoastalobservatory.org.uk](http://www.northeastcoastalobservatory.org.uk)). Wind  
545 data are courtesy of the Met Office (2006). Many thanks to the National Trust and David Barker for  
546 permission to use and regularly access the study site, and to Samantha Waugh and David Hodgson  
547 for help with fieldwork. Thanks also to Jess Benjamin and Zuzanna Swirad for assistance in producing  
548 Fig. 1. We thank A Young and M Dickson for their constructive and insightful review of our  
549 manuscript.

550

## 551 **References**

552 Adams, P. N., Storlazzi, C. D., Anderson, R. S., 2005. Nearshore wave-induced cyclical flexing of sea  
553 cliffs. *Journal of Geophysical Research-Earth Surface*, 110, F02002, 10.1029/2004JF000217

554

555 Ashford, S.A., Sitar, N., Lysmer, J., Deng, N., 1997. Topographic effects on the seismic response of  
556 steep slopes. *Bulletin of the Seismological Society of America*, 87(3), 701-709

557

558 Battjes, J.A., Stive, M.J.F., 1985. Calibration and verification of a dissipation model for random  
559 breaking waves. *Journal of Geophysical Research-Oceans*, 90(NC5), 9159-9167,  
560 10.1029/JC090iC05p09159

561

562 Beetham, E.P., Kench, P.S., 2011. Field observations of infragravity waves and their behaviour on  
563 rock shore platforms. *Earth Surface Processes and Landforms*, 36(14), 1872-1888, 10.1002/esp.2208

564

565 Bormann, P. (Ed.), 2009. New manual of seismological observatory practise (NMSOP-1). IASPEI, GFZ  
566 German research centre for geosciences, 10.2312/GFZ.NMSOP\_r1\_ch1

567

568 Bowman, D., Guillen, J., Lopez, L., Pellegrino, V., 2009. Planview Geometry and morphological  
569 characteristics of pocket beaches on the Catalan coast (Spain). *Geomorphology*, 108(3-4), 191-199,  
570 10.1016/j.geomorph.2009.01.005

571

572 Bray, M. J., Hooke, J. M. 1997. Prediction of soft-cliff retreat with accelerating sea-level rise. *Journal*  
573 *of Coastal Research*, 13, 453-467

574

575 Carter, R.W.G., Jennings, S.C., Orford, J.D., 1990. Headland erosion by waves. *Journal of Coastal*  
576 *Research*, 6(3), 517-529

577  
578 Dickson, M. E., Walkden, M. J. A., Hall, J. W., 2007. Systemic impacts of climate change on an eroding  
579 coastal region over the twenty-first century. *Climatic Change*, 84(2), 141-166, 10.1007/s10584-006-  
580 9200-9  
581  
582 Dickson, M. E., Pentney, R., 2012. Micro-seismic measurements of cliff motion under wave impact  
583 and implications for the development of near-horizontal shore platforms. *Geomorphology*, 151-152,  
584 27-38, 10.1016/j.geomorph.2012.01.006  
585  
586 Earlie, C.S., Young, A.P., Masselink, G., Russell, P.E., 2015. Coastal cliff ground motions and response  
587 to extreme storm waves. *Geophysical Research Letters*, 42(3), 847-854, 10.1002/2014gl062534  
588  
589 Friedrich, A., Kruger, F., Klinge, K., 1998. Ocean-generated microseismic noise located with the  
590 Grafenberg array. *Journal of Seismology*, 2, 47-64  
591  
592 Hapke, C.J., Reid, D., Richmond, B., 2009. Rates and Trends of Coastal Change in California and the  
593 Regional Behavior of the Beach and Cliff System. *Journal of Coastal Research*, 25(3), 603-615,  
594 10.2112/08-1006.1  
595  
596 Hedlin, M.A.H., Orcutt, J.A., 1989. A comparative study of island, seafloor, and subseafloor ambient  
597 noise-levels. *Bulletin of the Seismological Society of America*, 79, 172-179.  
598  
599 Klein, A.H.D., de Menezes, J.T., 2001. Beach morphodynamics and profile sequence for a Headland  
600 Bay Coast. *Journal of Coastal Research*, 17(4), 812-835  
601  
602 Komar, P.D., 1997. *Beach processes and sedimentation*. Prentice Hall, Upper Saddle River, N.J.  
603  
604 Komar, P.D., 1985. Computer models of shoreline configuration: headland erosion and the graded  
605 beach revisited. In: M.J. Woldenberg (Ed.), *Models in Geomorphology*. Allen and Unwin, London, pp.  
606 139-154  
607  
608 Limber, P.W., Murray, A.B., 2011. Beach and sea-cliff dynamics as a driver of long-term rocky  
609 coastline evolution and stability. *Geology*, 39(12), 1147-1150, 10.1130/G32315.1  
610

611 Limber, P.W., Murray, A.B., Adams, P.N., Goldstein, E.B., 2014. Unraveling the dynamics that scale  
612 cross-shore headland relief on rocky coastlines: 1. Model development. *Journal of Geophysical*  
613 *Research-Earth Surface*, 119(4), 854-873.10.1002/2013jf002950  
614  
615 Longuet-Higgins, M. S., 1950. A theory of the origin of microseisms. *Philosophical Transactions of the*  
616 *Royal Society of London. Series A, Mathematical and Physical*, 243, 1-35  
617  
618 Lowrie, W., 1997. *Fundamentals of geophysics*. Cambridge University Press, Cambridge ; New York,  
619 NY, USA  
620  
621 Marshall, R.J.E., Stephenson, W.J., 2011. The morphodynamics of shore platforms in a micro-tidal  
622 setting: Interactions between waves and morphology. *Marine Geology*, 288(1-4), 18-31,  
623 10.1016/j.margeo.2011.06.007  
624  
625 Mavko, G., Mukerji, T., Dvorkin, J., 1998. *The rock physics handbook: tools for seismic analysis in*  
626 *porous media*. Cambridge University Press, Cambridge  
627  
628 Messaoudi, A., Laouami, N., Mezour, N., 2012. Topographic effects on the seismic responses of  
629 slopes. *Proceedings of the 15th World Conference on Earthquake Engineering*, Lisbon, Portugal  
630  
631 Met Office (2006): MIDAS: UK Hourly Weather Observation Data. NCAS British Atmospheric Data  
632 Centre, accessed 26/03/18. <http://catalogue.ceda.ac.uk/uuid/916ac4bbc46f7685ae9a5e10451bae7c>  
633  
634 Murray, A. B., Ashton, A. D. 2013. Instability and finite-amplitude self-organization of large-scale  
635 coastline shapes. *Philosophical Transactions of The Royal Society*, 371: 20120363,  
636 10.1098/rsta.2012.0363  
637  
638 Norman, E.C., Rosser, N.J., Brain, M.J., Petley, D.N., Lim, M., 2013. Coastal cliff-top ground motions  
639 as proxies for environmental processes. *Journal of Geophysical Research-Oceans*, 118(12), 6807-  
640 6823, 10.1002/2013jc008963  
641  
642 Ogawa, H., Dickson, M.E., Kench, P.S., 2011. Wave transformation on a sub-horizontal shore  
643 platform, Tatapouri, North Island, New Zealand. *Continental Shelf Research*, 31(14), 1409-1419,  
644 10.1016/j.csr.2011.05.006

645  
646 Ogawa, H., Dickson, M.E., Kench, P.S., 2016. Generalised observations of wave characteristics on  
647 near-horizontal shore platforms: Synthesis of six case studies from the North Island, New Zealand.  
648 *New Zealand Geographer*, 72(2), 107-121, 10.1111/nzg.12121  
649  
650 Poate, T., Masselink, G., Austin, M., Dickson, M., Kench, P., 2016. Observation of Wave  
651 Transformation on Macro-tidal Rocky Platforms. *Journal of Coastal Research*, 602-606, 10.2112/si75-  
652 121.1  
653  
654 Sallenger, A.H., Krabill, W., Brock, J., Swift, R., Manizade, S., Stockdon, H., 2002. Sea-cliff erosion as a  
655 function of beach changes and extreme wave runup during the 1997-1998 El Nino. *Mar. Geol.*,  
656 187(3-4), 279-297, 10.1016/s0025-3227(02)00316-x  
657  
658 Stein, S., Wysession, M., 2003. An introduction to seismology, earthquakes, and earth structure.  
659 Blackwell, Oxford  
660  
661 Stephenson, W.J., Kirk, R.M., 2000. Development of shore platforms on Kaikoura Peninsula, South  
662 Island, New Zealand - Part one: The role of waves. *Geomorphology*, 32(1-2), 21-41, 10.1016/S0169-  
663 555X(99)00061-6  
664  
665 Stephenson, W.J., Naylor, L.A., Smith, H., Chen, B., Brayne, R.P., 2017. Wave transformation across a  
666 macrotidal shore platform under low to moderate energy conditions. *Earth Surface Processes and*  
667 *Landforms*, 10.1002/esp.4245  
668  
669 Sunamura, T., 1976. Feedback relationship in wave erosion of laboratory rocky coast. *Journal of*  
670 *Geology*, 84(4), 427-437, 10.1086/628209  
671  
672 Sunamura, T., 1977. Relationship between wave-induced cliff erosion and erosive force of waves.  
673 *Journal of Geology*, 85(5), 613-618, 10.1086/628340  
674  
675 Sunamura, T., 1982. A wave tank experiment on the erosional mechanism at a cliff base. *Earth*  
676 *Surface Processes and Landforms*, 7(4), 333-343, 10.1002/esp.3290070405  
677

678 Sunamura, T., 1992. Geomorphology of rocky coasts. Coastal morphology and research. J. Wiley,  
679 Chichester; New York  
680

681 Trenhaile, A.S., 1987. The geomorphology of rock coasts. Oxford research studies in geography.  
682 Clarendon Press, Oxford  
683

684 Trenhaile, A. S., Kanyaya, J. I. 2007. The role of wave erosion on sloping and horizontal shore  
685 platforms in macro- and mesotidal environments. Journal of Coastal Research, 23, 298-309,  
686 10.2112/04-0282.1  
687

688 Trenhaile, A. S. 2011. Predicting the response of hard and soft rock coasts to changes in sea level and  
689 wave height. Climatic Change, 109, 599-615, 10.1007/s10584-011-0035-7  
690

691 Vann Jones, E.C., Rosser, N.J., Brain, M.J., Petley, D.N., 2015. Quantifying the environmental controls  
692 on erosion of a hard rock cliff. Marine Geology, 363, 230-242, 10.1016/j.margeo.2014.12.008  
693

694 Walkden, M.J.A., Hall, J.W., 2005. A predictive Mesoscale model of the erosion and profile  
695 development of soft rock shores. Coastal Engineering, 52(6), 535-56,  
696 10.1016/j.coastaleng.2005.02.005  
697

698 Young, A.P., Adams, P.N., O'Reilly, W.C., Flick, R.E., Guza, R.T., 2011. Coastal cliff ground motions  
699 from local ocean swell and infragravity waves in southern California. Journal of Geophysical  
700 Research-Oceans, 116, C09007, 10.1029/2011jc007175  
701

702 Young, A.P., Guza, R.T., Adams, P.N., O'Reilly, W.C., Flick, R.E., 2012. Cross-shore decay of cliff top  
703 ground motions driven by local ocean swell and infragravity waves. Journal of Geophysical Research-  
704 Oceans, 117, 10.1029/2012jc007908  
705

706 Young, A.P., Guza, R.T., Dickson, M. E., O'Reilly, W.C., Flick, R.E., 2013. Ground motions on rocky,  
707 cliffed, and sandy shorelines generated by ocean waves. Journal of Geophysical Research-Oceans,  
708 118, 10.1002/2013JC008883  
709

710 Young, A.P., Guza, R.T., O'Reilly, W.C., Burvingt, O., Flick, R.E., 2016. Observations of coastal cliff base  
711 waves, sand levels, and cliff top shaking. *Earth Surface Processes and Landforms*, 41(11), 1564-1573,  
712 10.1002/esp.3928

713

#### 714 **Figure captions**

715

716 **Figure 1:** Study site location. a) Location of the study site on the North Yorkshire coast, UK. b) The  
717 study site lies to the east of the village of Staithes and consists of two headlands and one bay  
718 (highlighted by the dashed box). The foreshore exposed at mean low spring tide is shown. c) DEM of  
719 the studied bay and headlands showing foreshore elevations above mean low spring tide. The  
720 locations of the seven seismometers are denoted by the stars: ES01 – ES07 moving west to east. The  
721 grey lines indicate the positions of the foreshore profiles in front of each seismometer shown in  
722 Figure 2. The black contour is at 1 m OD and elevation below this is shaded at 0.25 m intervals until  
723 the mean low spring tide elevation at -2 m OD. d) Aerial photo of the study site taken on 09/12/2017  
724 1 hour 14 minutes after the high spring tide. Tidal elevation at the Whitby tide gauge was 1.5 m OD,  
725  $H_s$  recorded at the Whitby wave buoy was 4.3 m and wave direction was NNE.

726

727 **Figure 2:** Cliff and foreshore profiles at the seismometer locations: a) ES01; b) ES02; c) ES03; d) ES04;  
728 e) ES05; f) ES06; g) ES07. The stars denote the position of the seismometer at the cliff top. Detail of  
729 the foreshore profiles used within the wave model at: h) ES01; i) ES02; j) ES03; k) ES04; l) ES05; m)  
730 ES06; n) ES07. Tidal elevations recorded at the Whitby tide gauge are shown: highest astronomical  
731 tide (HAT), mean high water spring (MHWS), mean high water neap (MHWN), mean low water neap  
732 (MLWN), mean low water spring (MLWS). The foreshore profiles extend to the MLWS elevation.

733

734 **Figure 3:** Power spectrograms of cliff ground motion for the seven seismometers, tide and wave  
735 heights and wave directions for the monitoring period 29/11/2013 – 20/07/2014. a – g) Power  
736 spectrograms of the vertical (Z) cliff motions for the seismometers' frequency response range (0.03 –  
737 180 s/33.3 – 0.0055 Hz). Power is presented in decibels (dB) calculated as  $10 \log_{10}((\text{ms}^{-1})^2/\text{Hz})$ . Three  
738 distinct bands of ground motions are identified in each spectrogram: long-periods (LP) (>20 s/<0.05  
739 Hz) (black box); microseisms (MS) (1-20 s/1-0.05 Hz) (red box); and high frequency shaking (HT)  
740 caused by wave impacts at the cliff toe during high tides (0.03 – 0.3 s/3.33 – 33.33 Hz) (blue box).  
741 The white zones indicate data gaps. a) ES01. b) ES02. c) ES03. d) ES04. e) ES05. f) ES06. g) ES07. h)  
742 Tide heights and residuals monitored at the Whitby tide gauge approximately 13 km south east of  
743 the field site. i) Significant wave heights ( $H_s$ ) and j) wave direction frequency (%) monitored at the

744 Whitby wave buoy, approximately 13 km south east of the study site, 1.5 km offshore and in  
745 approximately 17 m water depth. At ES01 there is a persistent band of noise at 10 – 20 Hz, of  
746 approximately - 75dB, the steady nature of which suggests mechanical noise. Wave and tide data are  
747 courtesy of the North East Coastal Observatory ([www.northeastcoastalobservatory.org.uk](http://www.northeastcoastalobservatory.org.uk)).

748

749 **Figure 4:** Relationships between the wave pressure sensor (WPS) and the wave model significant  
750 wave heights ( $H_s$ ) for a subsequent study (13-day duration, 20 Feb – 4 Mar 2015) at: a) ES01; b) ES04;  
751 c) ES06; and d) all three sites combined. Statistically significant relationships are presented (at  $p$ -  
752 value  $\geq 0.05$ ).

753

754 **Figure 5:** Time series of spring tides during: a-i) (first column) a storm occurring on 05-06/12/13; and  
755 j-r) (second column) less energetic conditions on 03/03/14. a-g & j-p) Spectrograms of the power  
756 spectral density across the seven seismometers (dB calculated as  $10 \log_{10}((\text{ms}^{-1})^2/\text{Hz})$ ) for the Z  
757 component, within the period/frequency range 0.03 – 180 s / 33.3 – 0.0055 Hz, at a & j) ES01; b & k)  
758 ES02; c & l) ES03; d & m) ES04; e & n) ES05; f & o) ES06; g & p) ES07; h & q) concurrent tide and  
759 combined tide and wave elevation at the cliff toe ( $h_{elevation}$ ) modelled for East Staithes; and i & r)  
760 significant wave height ( $H_s$ ) and maximum wave height ( $H_{max}$ ) recorded at the Whitby wave buoy,  
761 and wind velocity measured at Loftus (5 km from study site). Wave and tide data are courtesy of the  
762 North East Coastal Observatory ([www.northeastcoastalobservatory.org.uk](http://www.northeastcoastalobservatory.org.uk)). Wind data are courtesy  
763 of the Met Office (2006).

764

765 **Figure 6:** Time series of neap tides during: a-i) (first column) a storm occurring on 26-27/03/14; and  
766 j-r) (second column) less energetic conditions on 10/04/14. a-g & j-p) Spectrograms of the power  
767 spectral density across the seven seismometers (dB calculated as  $10 \log_{10}((\text{ms}^{-1})^2/\text{Hz})$ ) for the Z  
768 component, within the period/frequency range 0.03 – 180 s / 33.3 – 0.0055 Hz, at a & j) ES01; b & k)  
769 ES02; c & l) ES03; d & m) ES04; e & n) ES05; f & o) ES06; g & p) ES07; h & q) concurrent tide and  
770 combined tide and wave elevation at the cliff toe ( $h_{elevation}$ ) modelled for East Staithes; and i & r)  
771 significant wave height ( $H_s$ ) and maximum wave height ( $H_{max}$ ) recorded at the Whitby wave buoy,  
772 and wind velocity measured at Loftus (5 km from study site). Wave and tide data are courtesy of the  
773 North East Coastal Observatory ([www.northeastcoastalobservatory.org.uk](http://www.northeastcoastalobservatory.org.uk)). Wind data are courtesy  
774 of the Met Office (2006).

775



776 **Figure 7:** Various statistics of *HT* ground motion energy ( $(\mu\text{m s}^{-1})^2$ ) for each of the seven instruments  
777 over the monitoring period 29/11/2013 to 20/07/2014: a) total *HT* ground motion energy over the  
778 monitoring period (*Total*); b) hourly maximum ( $Max_h$ ); c) 99<sup>th</sup> percentile of the  $Max_h$ .

779

780 **Figure 8:** Distributions of water level inundation frequency and total *HT* ground motion energy over  
781 the monitoring period (*Total*) up the cliff profile within the inundation zone during the monitoring  
782 period 29/11/2013 – 20/07/2014 for each of the seismometer locations: a & b) ES01; c & d) ES02; e  
783 & f) ES03; g & h) ES04; i & j) ES05; k & l) ES06; m & n) ES07. Inundation frequency (percentage) of  
784 tide-only (black line) and combined tide and wave elevation at the cliff toe ( $h_{elevation}$ ) (grey bars) for  
785 0.1 m bins of cliff elevation (a, c, e, g, i, k, m). The foreshore profile exposed at low spring tide is  
786 shown by the grey line. *Total* (black bars, Z component, 3 – 33 Hz) per 0.1 m elevation bin of  $h_{elevation}$   
787 inundation (b, d, f, h, j, l, n). The dashed grey line shows the elevation of the cliff toe.

788

789 **Figure 9:** Relationships between total *HT* ground motion energy over the monitoring period (*Total*)  
790 and foreshore and cliff characteristics: a) cliff toe elevation; b) number of steps in foreshore; c)  
791 foreshore elevation change; d) seismometer – cliff toe distance along cliff surface; e) linear distance  
792 between seismometer – cliff toe; f) mean cliff slope; and g) maximum cliff slope. Statistically  
793 significant relationships are presented (at  $p$ -value  $\geq 0.05$ ). Foreshore width and cliff height were  
794 also regressed against *Total* however were not statistically significant.

795

796 **Figure 10:** Scatter plots of the relationship between hourly total *HT* ground motion energy ( $Total_h$ )  
797 and combined tide and wave height above the cliff toe ( $h_{height}$ ) at the seven sites: a) ES01; b) ES02; c)  
798 ES03; d) ES04; e) ES05; f) ES06; g) ES07. Colour corresponds to modelled cliff toe wave height (m).

799

Figure 1

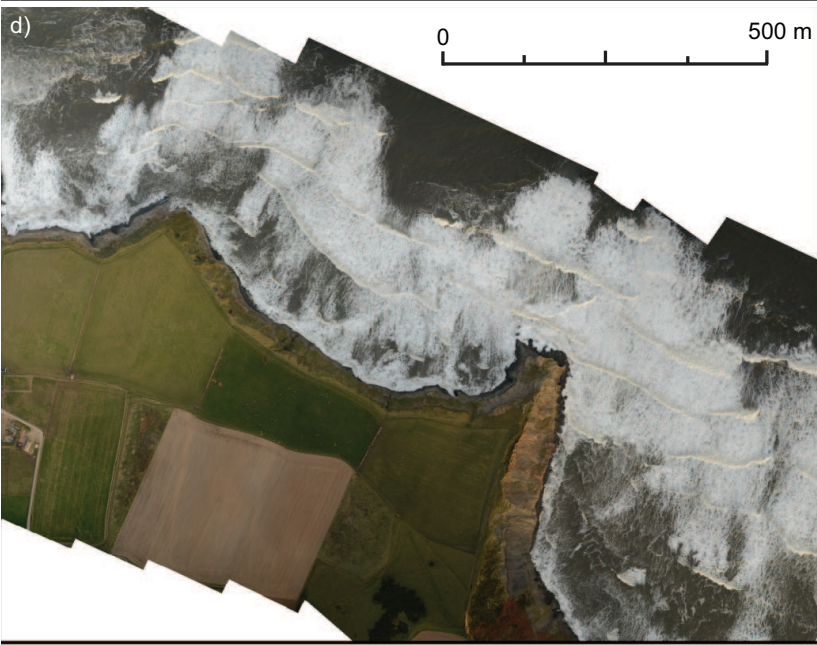
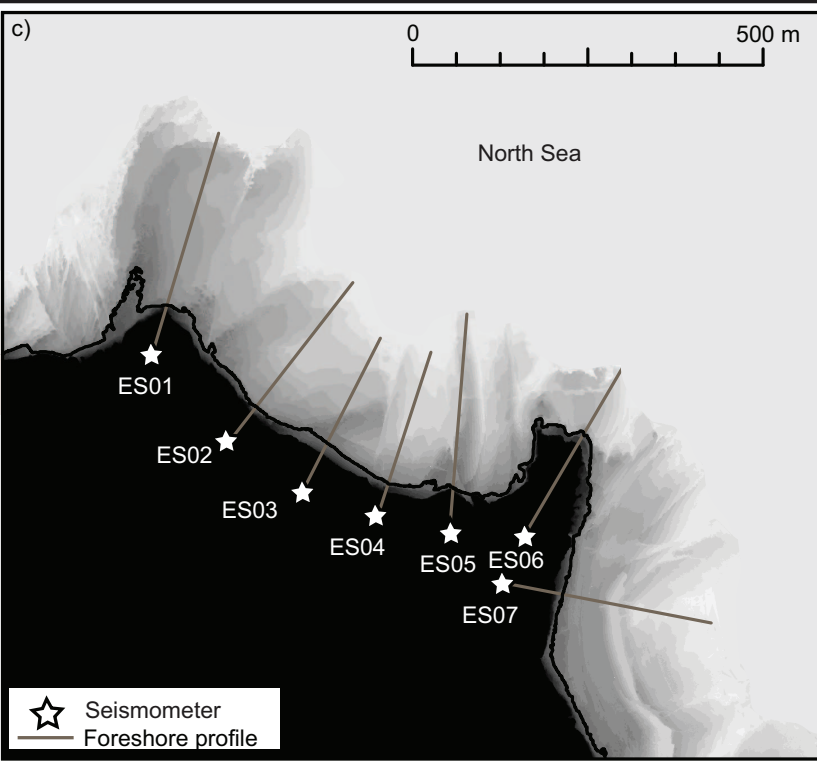
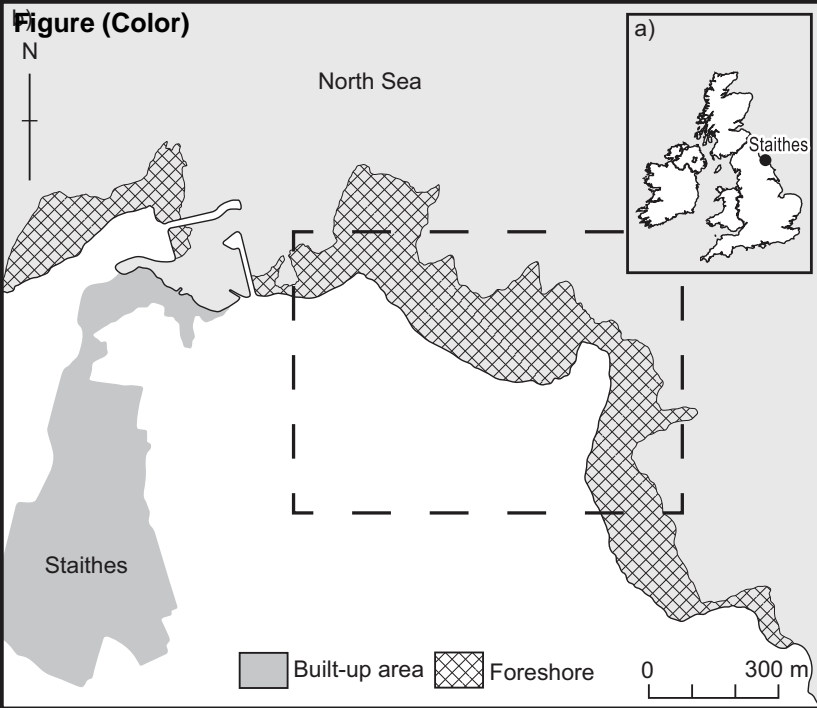


Figure 2

**Figure (Greyscale)**

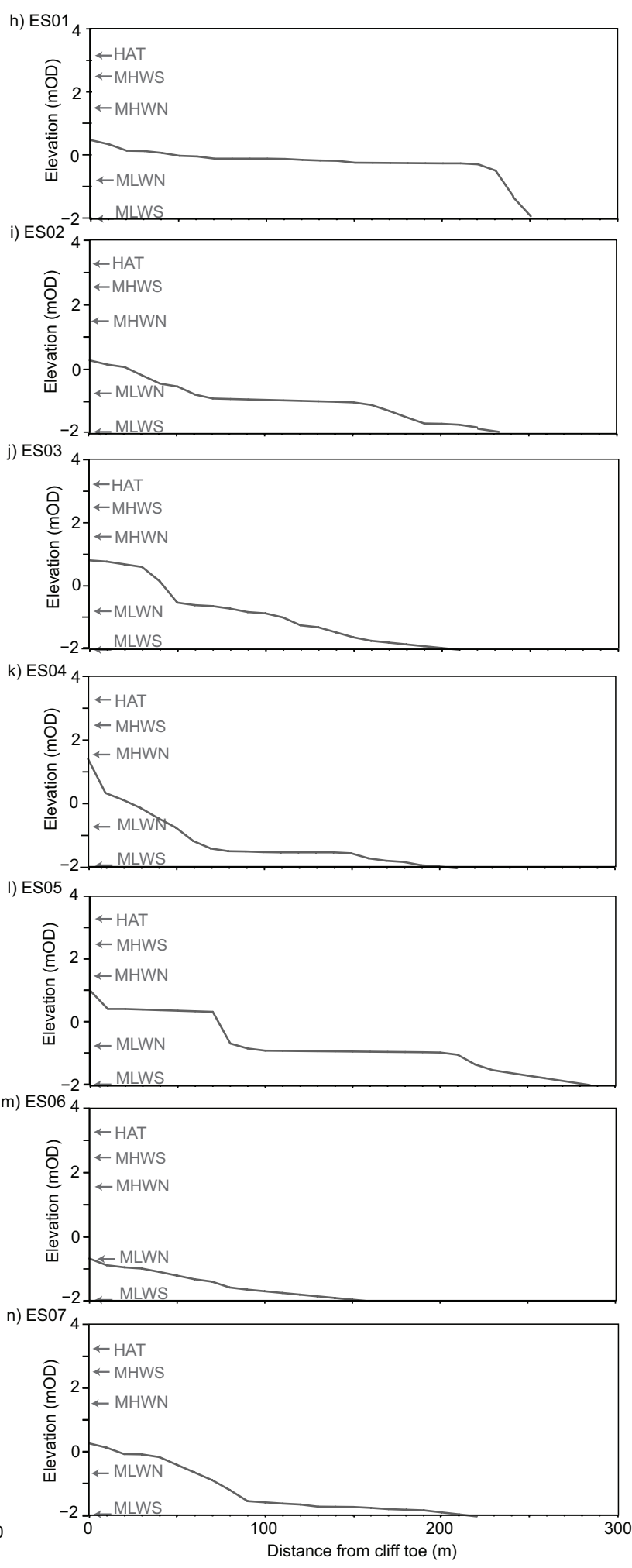
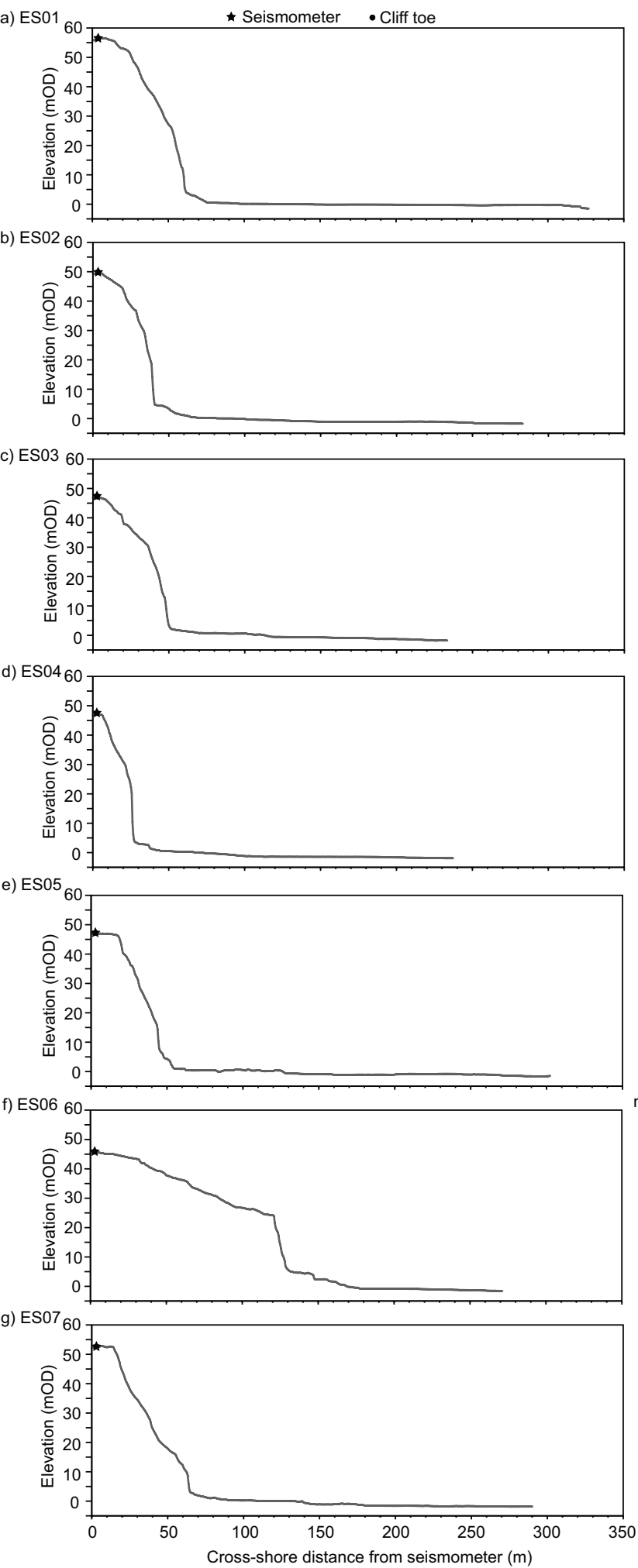
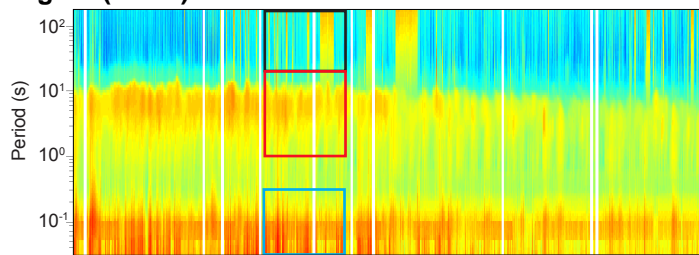
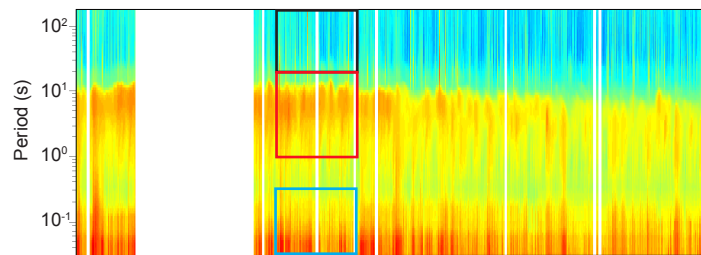


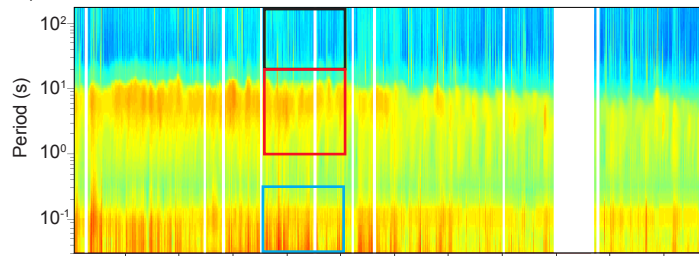
Figure 3

**Figure (Color)**

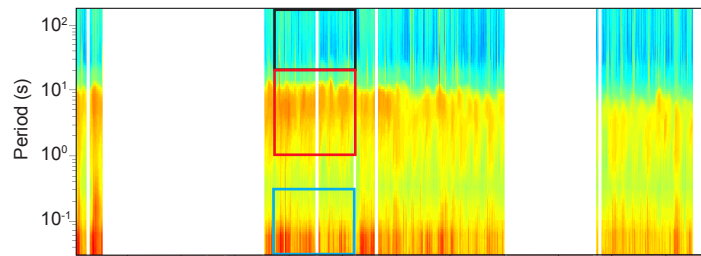
f) ES06



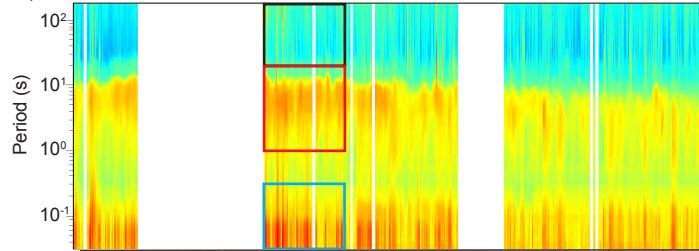
b) ES02



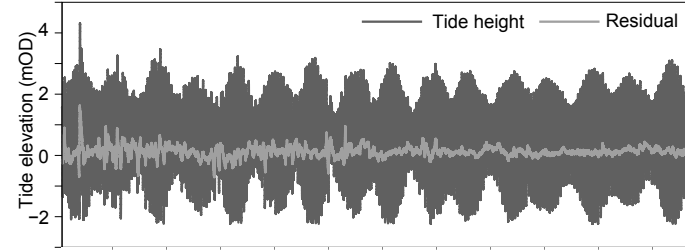
g) ES07



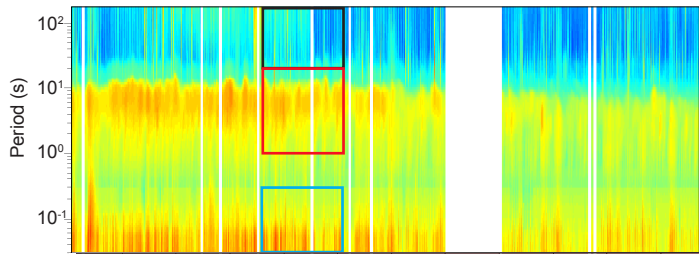
c) ES03



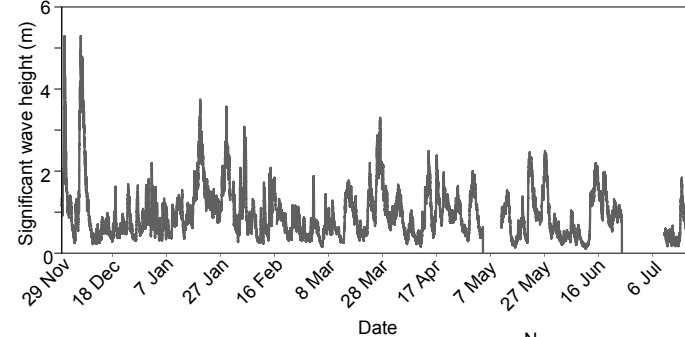
h) Tide heights



d) ES04



i) Wave heights



e) ES05

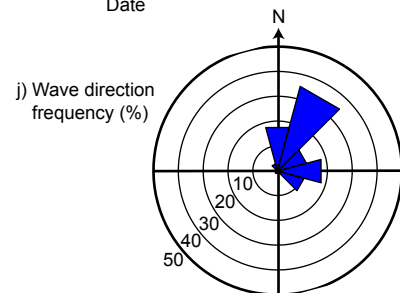
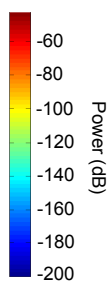
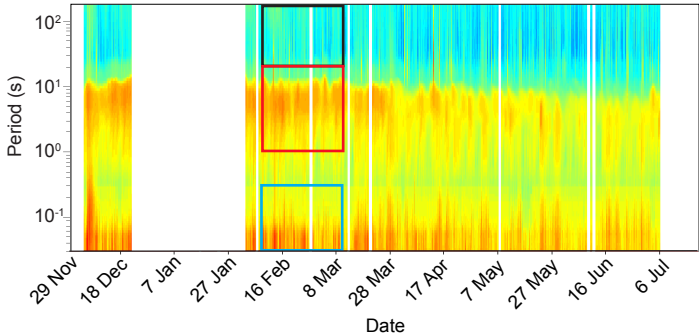
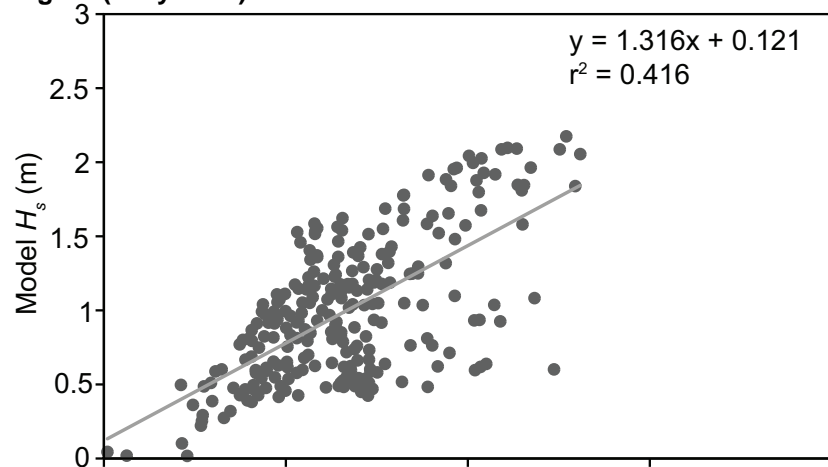


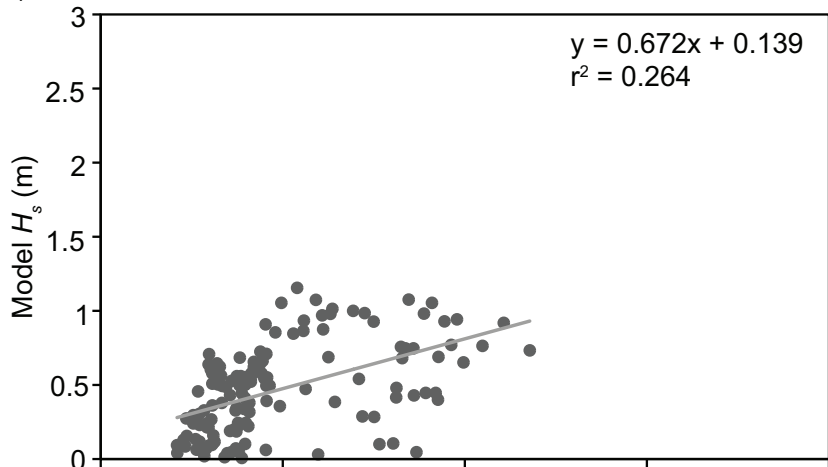
Figure 4



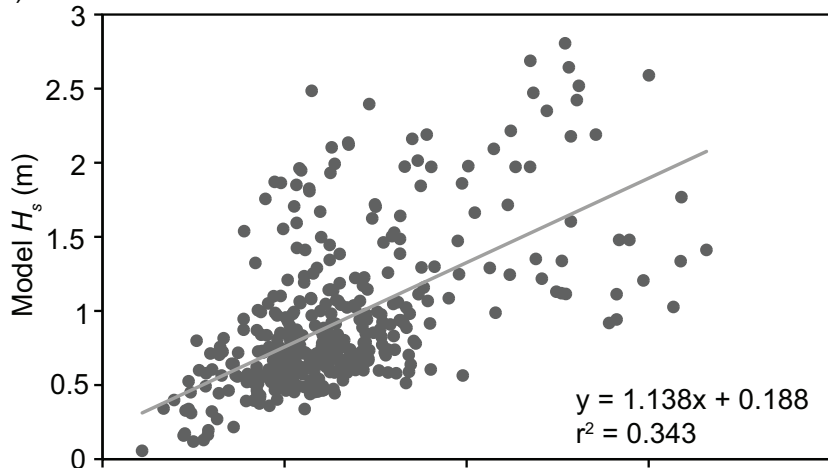
a) SS01  
Figure (Greyscale)



b) ES04



c) ES06



d) All three sites combined

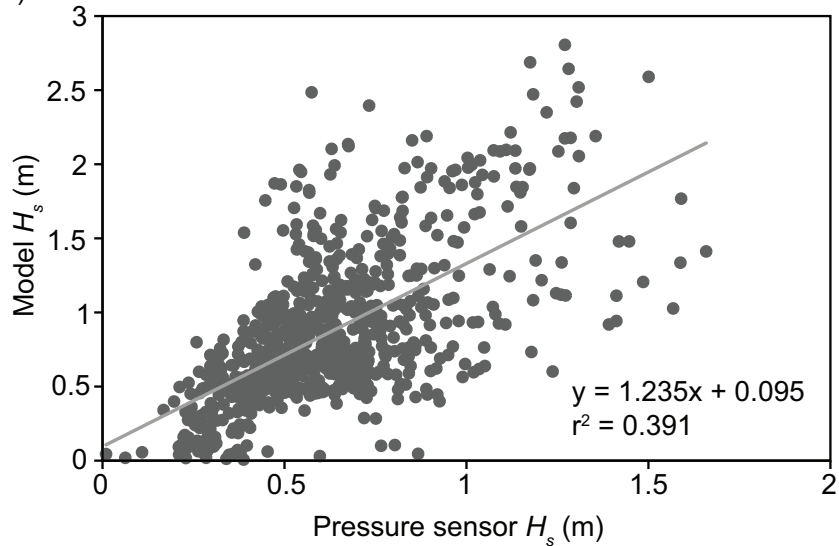


Figure 5

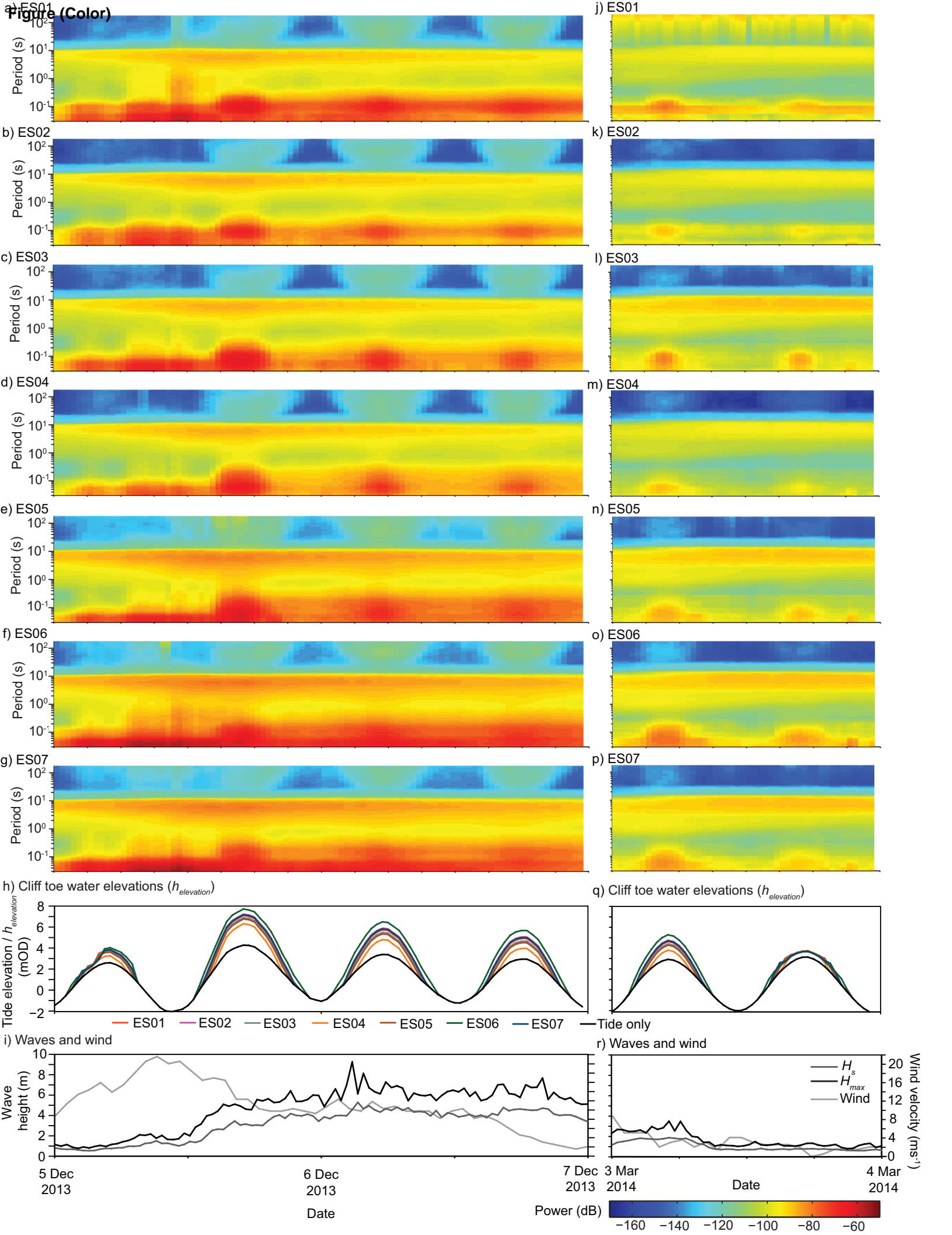


Figure 6

**Figure (Color)**

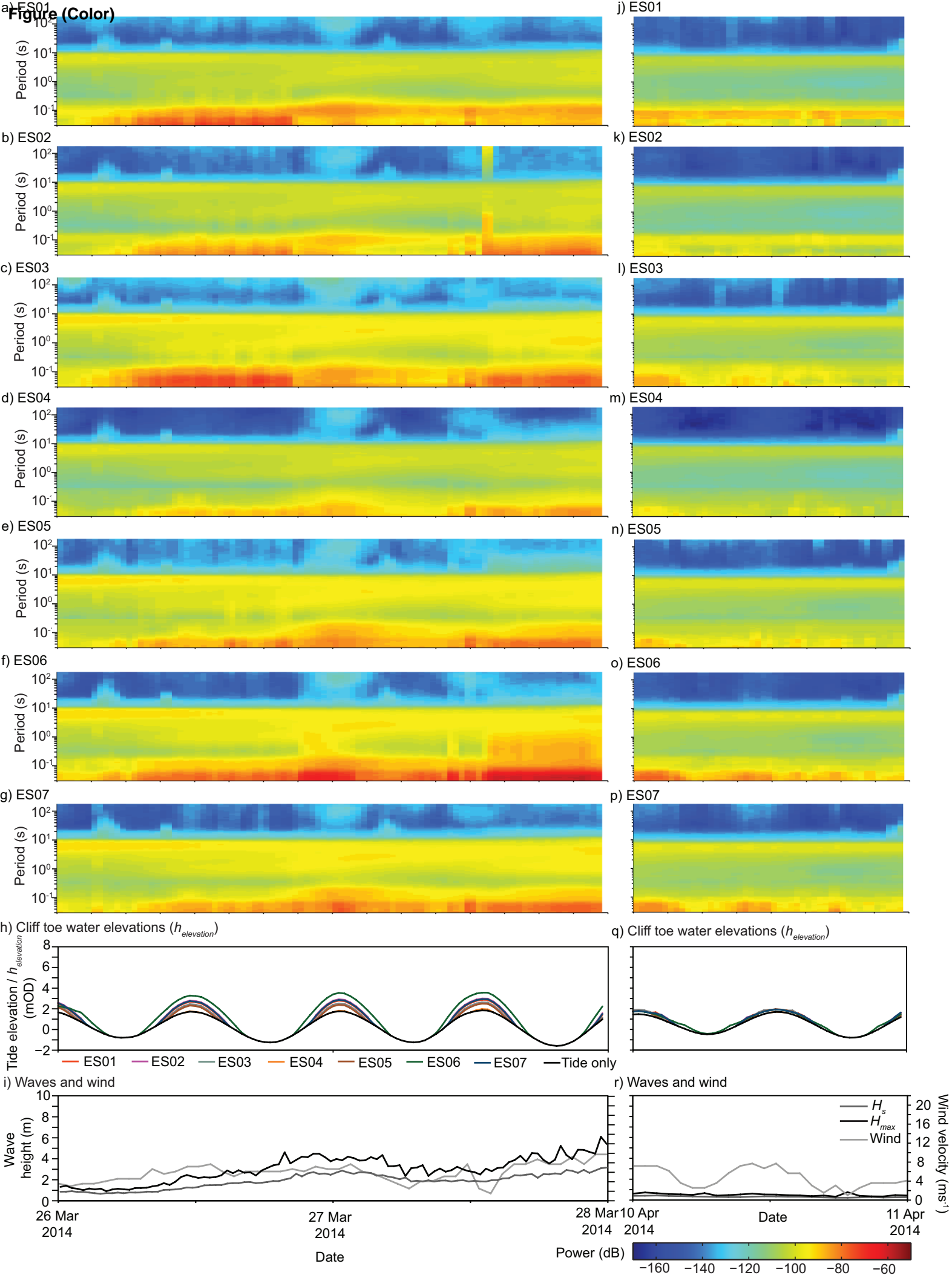


Figure 7

Figure 10 (Greyscale)

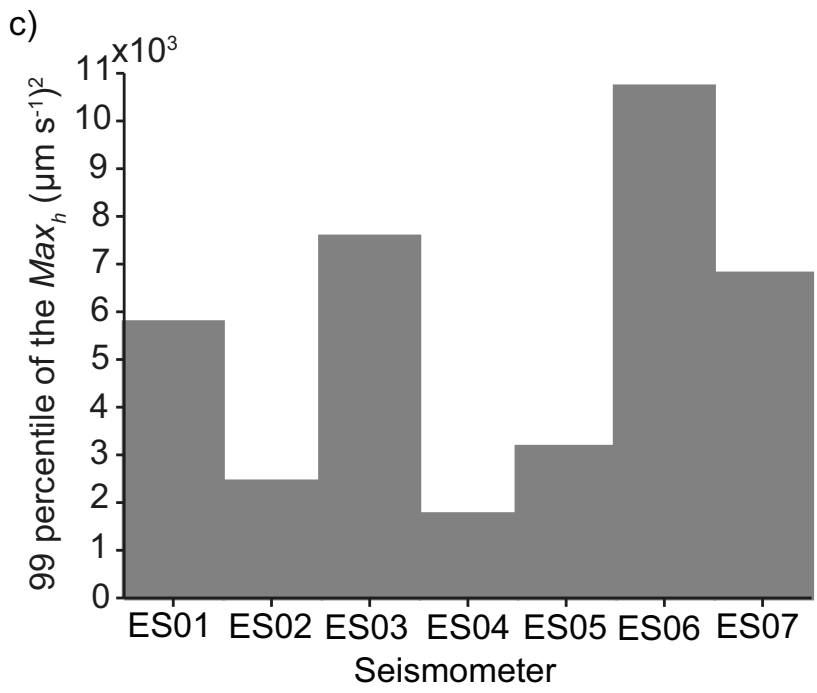
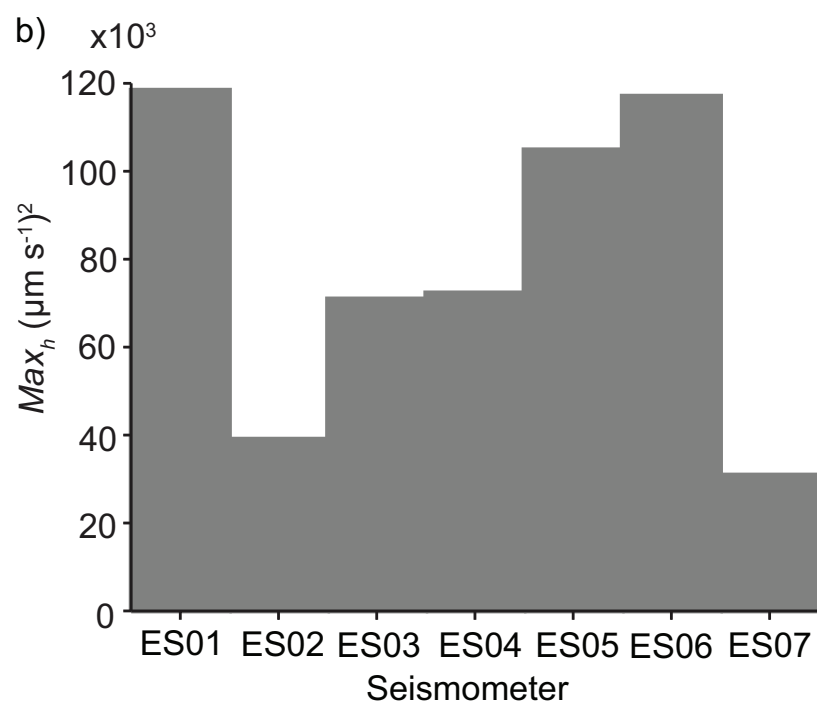
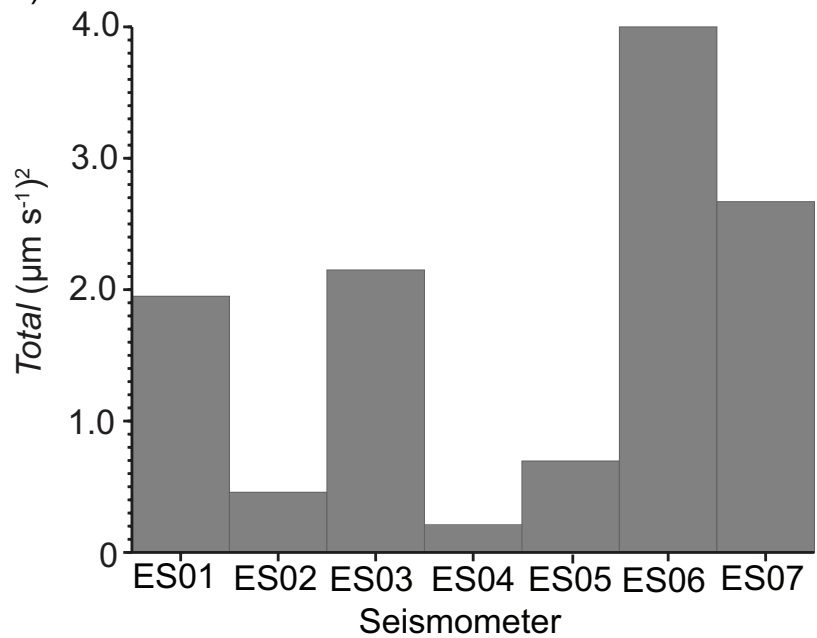


Figure 8



**Figure (Greyscale)**

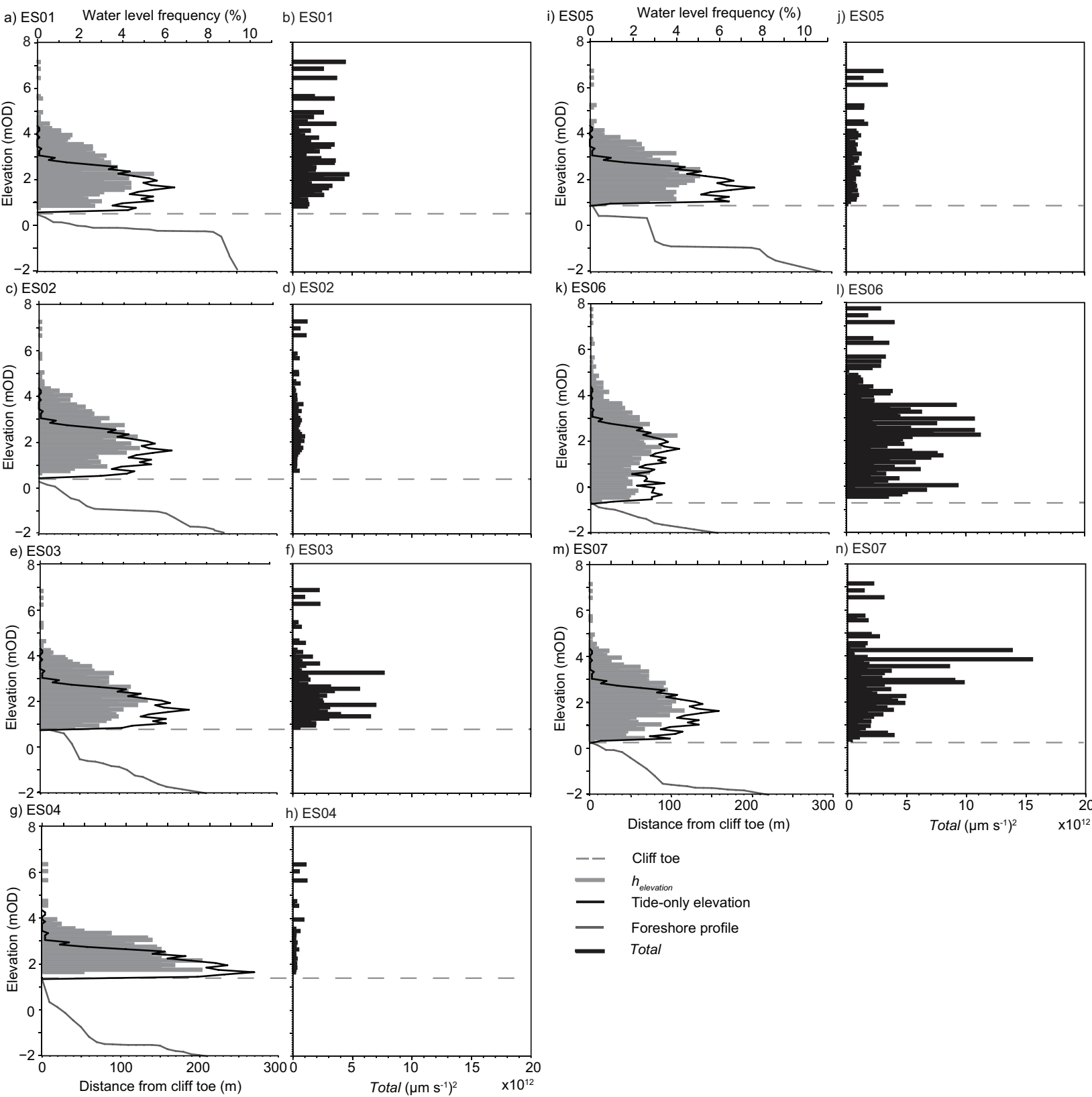
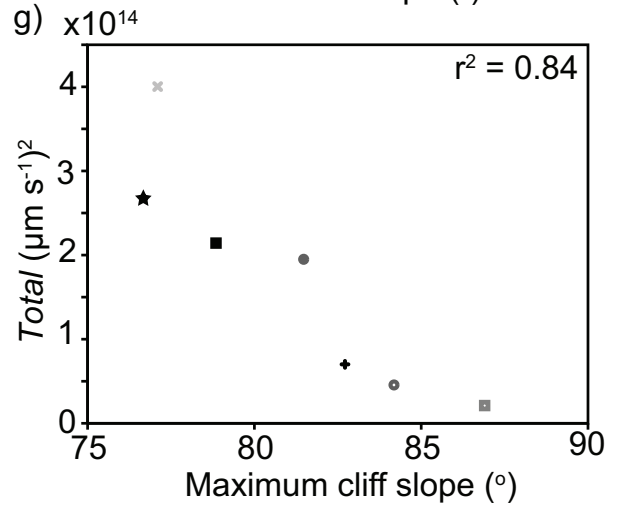
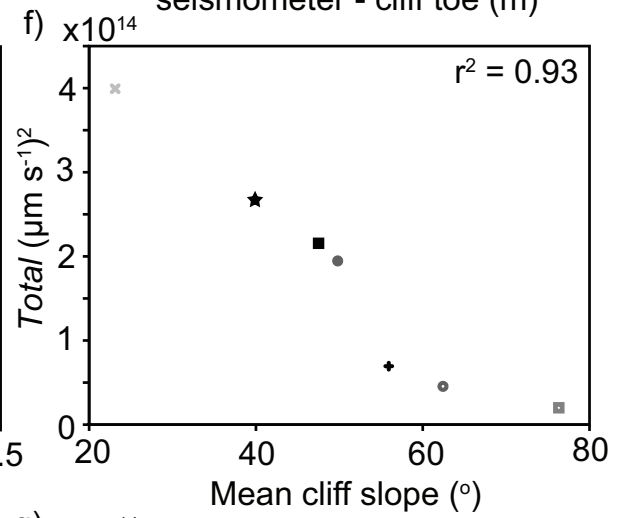
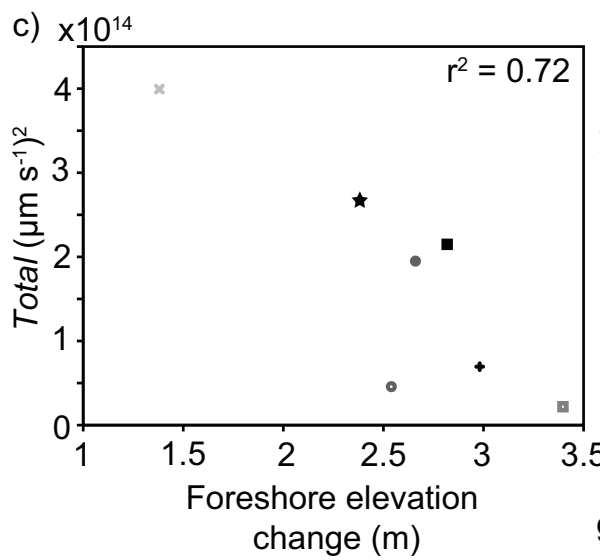
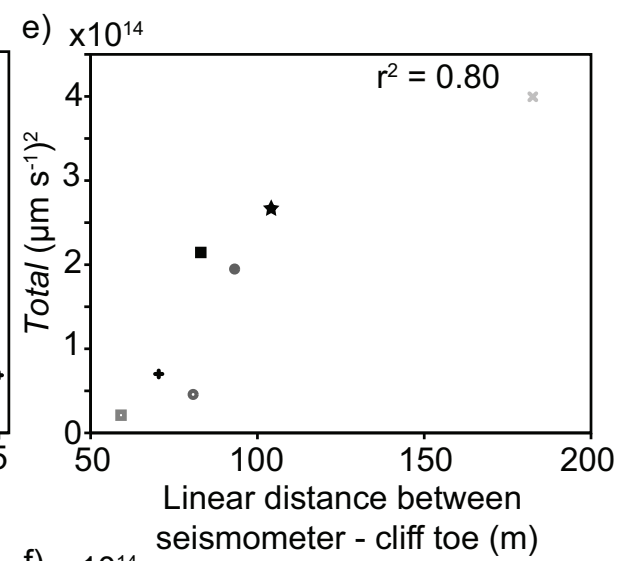
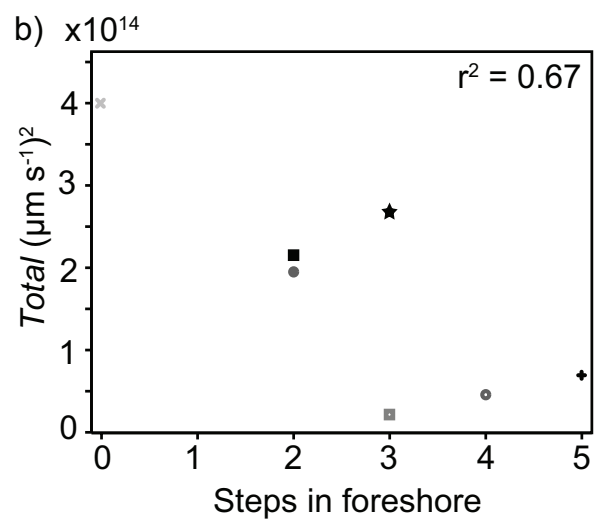
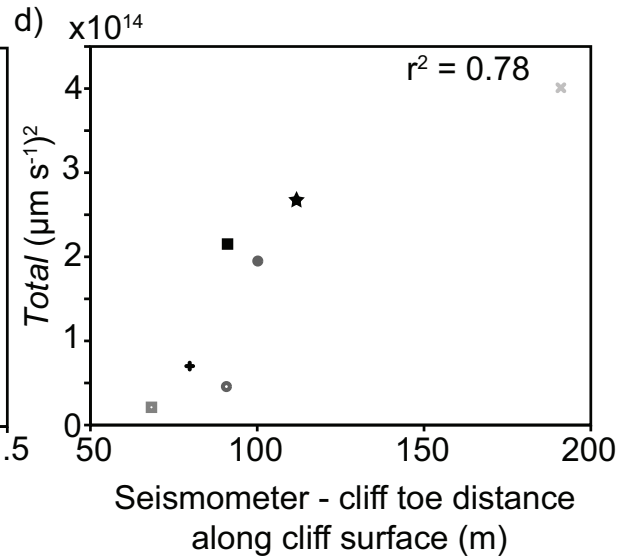
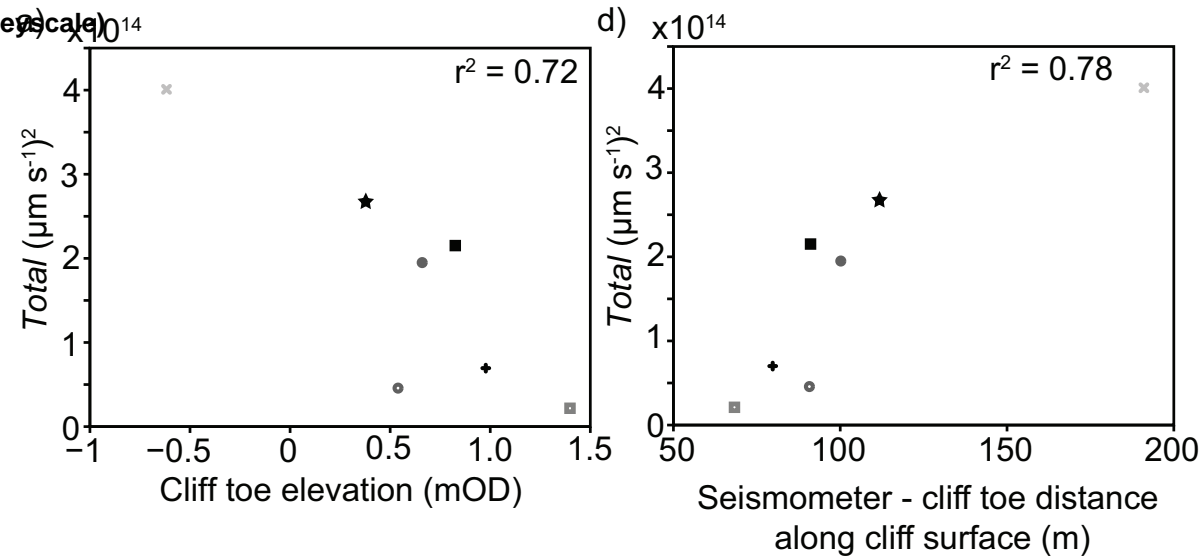


Figure 9

Figure (Grey scale)



- ES01    ◦ ES02
- ES03    ◻ ES04
- + ES05    × ES06
- ★ ES07

Figure 10

Figure (Color)

